Title

Increased Excitation-Inhibition Ratio Stabilizes Synapse and Circuit Excitability in Four Autism Mouse Models

Journal

Neuron, 101(4)

ISSN

0896-6273

Authors

Antoine, Michelle W
Langberg, Tomer
Schnepel, Philipp
et al.

Publication Date

2019-02-01

DOI

10.1016/j.neuron.2018.12.026

Peer reviewed

HHS Public Access

Author manuscript

Neuron. Author manuscript; available in PMC 2020 February 20.

Published in final edited form as:

Neuron. 2019 February 20; 101(4): 648–661.e4. doi:10.1016/j.neuron.2018.12.026.

Increased excitation-inhibition ratio stabilizes synapse and circuit excitability in four autism mouse models

Michelle W. Antoine[*,†], **Tomer Langberg**[*], **Philipp Schnepel**[2,*], **Daniel E. Feldman**[†,1]

Dept. of Molecular and Cellular Biology and Helen Wills Neuroscience Institute, UC Berkeley, Berkeley, CA 94720

Summary

Distinct genetic forms of autism are hypothesized to share a common increase in excitation-inhibition (E-I) ratio in cerebral cortex, causing hyperexcitability and excess spiking. We provide a systematic test of this hypothesis across 4 mouse models (*Fmr1*$^{-/y}$, *Cntnap2*$^{-/-}$, *16p11.2*$^{del/+}$, *Tsc2*$^{+/-}$), focusing on somatosensory cortex. All autism mutants showed reduced feedforward inhibition in layer 2/3 coupled with more modest, variable reduction in feedforward excitation, driving a common increase in E-I conductance ratio. Despite this, feedforward spiking, synaptic depolarization and spontaneous spiking were largely normal. Modeling revealed that E and I conductance changes in each mutant were quantitatively matched to yield stable, not increased, synaptic depolarization for cells near spike threshold. Correspondingly, whisker-evoked spiking was not increased *in vivo*, despite detectably reduced inhibition. Thus, elevated E-I ratio is a common circuit phenotype, but appears to reflect homeostatic stabilization of synaptic drive, rather than driving network hyperexcitability in autism.

Keywords

E-I ratio; cerebral cortex; somatosensory cortex; circuit excitability; Fragile X; homeostasis

Introduction

Autism spectrum disorders (ASD) are a family of neurodevelopmental disorders characterized by social and communication deficits, restricted and repetitive behaviors or interests, and abnormal sensory responses (Geschwind 2009). ASD is highly genetically heterogeneous, with >100 identified risk genes with diverse functions in transcriptional regulation, protein synthesis and degradation, synapse function and synaptic plasticity.

[†]Co-corresponding authors. Correspondence should be addressed to: 142 Life Sciences Addition, # 3200, MCB Dept., University of California, Berkeley, Berkeley, CA 92093-3200, mwantoine@berkeley.edu, dfeldman@berkeley.edu.

Author Contributions

MA, TL, PS: Designed, performed and analyzed in vitro (MA) and in vivo (TL, PS) experiments. DF: Designed experiments and performed modeling. MA, TL, DF: Co-wrote paper.

[*]Equal authorship

[1]Lead contact

[2]Current address: Max Delbrück Center for Molecular Medicine, Berlin, Germany

Declaration of Interests

The authors declare no competing interests.

Whether genetically distinct forms of ASD share a common dysfunction at the neural circuit level remains unclear.

One long-standing model is that genetically distinct forms of ASD share a common increase in synaptic excitation to inhibition (E-I) ratio in cerebral cortex, which drives hyperexcitability, excess spiking and increased noise in cortical circuits. This is hypothesized to cause the cognitive and behavioral symptoms of autism (Nelson and Valakh, 2015, Rubenstein and Merzenich, 2003). Prior synaptic physiology studies using transgenic mouse models of ASD provide mixed support for this E-I ratio hypothesis. Many report reduced inhibition (Chao et al., 2010; Gibson et al., 2008; Han et al., 2012; Liang et al., 2015; Mao et al., 2015; Wallace et al., 2012), often coupled with a smaller decrease in synaptic excitation. However, others report a greater decrease in excitation than inhibition (Dani et al., 2005, Delattre et al., 2013, Unichenko et al., 2017, Wood and Shepherd, 2010), or increased inhibition (Harrington et al., 2016, Tabuchi et al., 2007). Variation across studies in brain area, cell type, ASD genotype, and physiological methods complicates identification of common synaptic and local circuit defects in ASD.

Critically, whether increased E-I ratio yields hyperexcitable cortical networks in ASD remains unclear. From basic biophysics, increased E-I conductance ratio does not necessarily drive stronger synaptic depolarization or spike probability. Some ASD mouse models show increased pyramidal (PYR) firing rate in some cortical areas in vivo (Peixoto et al., 2016, Rotschafer and Razak, 2013, Zhang et al., 2014), but most show no or modest changes (Dolen et al., 2007, Goncalves et al., 2013, He et al., 2017, O'Donnell et al., 2017, Wallace et al., 2017) or even reduced PYR firing (Banerjee et al., 2016, Durand et al., 2012, Garcia-Junco-Clemente et al., 2013, Unichenko et al., 2017), even when inhibitory neuron spiking is reduced (Berzhanskaya et al., 2016; Goel et al., 2018). In humans, increased network excitability is suggested by increased seizure prevalence in some forms of ASD, but seizures only occur in a subset of patients and EEG may be normal during ASD symptoms (Samra et al., 2017, Tuchman et al., 2010). Many ASD mouse mutants show clear behavioral phenotypes in the absence of spontaneous seizures or abnormal EEG (Dhamne et al., 2017, Goorden et al., 2007, Peñagarikano et al., 2011). Thus, whether E-I ratio is systematically altered across genetically distinct forms of autism, and whether this drives excess spiking in cortical circuits, remain unclear. Optogenetic manipulations of E-I ratio and spiking in prefrontal cortex induce and ameliorate social behavioral deficits, but this doesn't mean that elevated E-I ratio or excess spiking is the endogenous cause of social impairment in ASD mice (Yizhar et al., 2011, Selimbeyoglu et al., 2017).

We tested for common circuit defects in somatosensory cortex (S1) of four genetically distinct, well-validated mouse models of ASD (*Fmr1*$^{-/y}$, *Cntnap2*$^{-/-}$, *16p11.2*$^{del/+}$, *Tsc2*$^{+/-}$). S1 is a reasonable focus because tactile disturbances are common in ASD (Robertson and Baron-Cohen, 2017), and S1 excitatory and inhibitory circuits are well characterized. We studied the feedforward circuit from layer (L) 4 to L2/3 pyramidal (PYR) cells, which is the first step in intracortical sensory processing. L4-L2/3 feedforward excitation and inhibition are integrated by PYR cells to evoke sparse spiking. This feedforward inhibition is mediated by parvalbumin (PV) interneurons, which are implicated in ASD. We systematically tested each ASD mutant *in vitro* and *in vivo* for abnormal synaptic excitation and inhibition in L2/3

PYR cells, abnormal network spiking, and impaired sensory coding. *Fmr1*$^{-/y}$ mice have impaired inhibition in L4 (Gibson et al., 2008), and *Cntnap2*$^{-/-}$ mice have fewer PV interneurons (Vogt et al., 2017), but E-I ratio phenotypes in L2/3 are unknown in any of these mutants. Thus, these four mutants provide a strong test for general applicability of the E-I ratio hypothesis.

We found that all ASD mutants exhibited decreased inhibition and more weakly decreased excitation, yielding increased E-I conductance ratio. However, contrary to the E-I ratio hypothesis, synaptic conductance modeling showed that these E-I changes were quantitatively matched to preserve peak synaptic depolarization, not increase it. Accordingly, peak synaptic depolarization and spiking were remarkably normal in ASD mutants, *in vivo* and *in vitro*. Thus, increased E-I ratio appears to be a compensatory mechanism that stabilizes synaptic depolarization and spiking excitability, rather than causing circuit hyperexcitability, in these ASD genotypes.

Results

L4-L2/3 synaptic currents and E-I conductance ratio

We tested for abnormal synaptic currents in S1 slices from juvenile *Fmr1*$^{-/y}$, *Cntnap2*$^{-/-}$, *16p11.2* $^{del/+}$ and *Tsc2*$^{+/-}$ mice and age-matched wild type controls. We first measured L4-evoked feedforward excitatory and inhibitory currents (EPSCs and IPSCs) converging onto single L2/3 PYR cells (Figure 1A). EPSCs and IPSCs were separated in whole-cell voltage clamp by holding at −72 and 0 mV, the reversal potentials for excitation and GABA-A inhibition. L4-evoked IPSCs were blocked by NBQX and D-APV (to 2.7±1.6% of control, n=3 cells), and thus represent disynaptic feedforward inhibition. For each PYR cell, we found the minimum L4 stimulation intensity required to evoke a detectable EPSC, denoted Eθ, and measured input-output curves for EPSCs and IPSCs at 1.0–1.5x Eθ. For analysis, currents were integrated over 20 ms, matching the time scale of L2/3 sensory integration *in vivo* (McGuire et al., 2014). Stimulation at Eθ generally evoked small EPSCs and IPSCs. Increasing stimulus intensity recruited disproportionately larger IPSCs, so that inhibition dominated at ≥ 1.2x Eθ, as in prior studies (House et al., 2011). Example cells for all genotypes are shown in Figure 1B.

Fmr1$^{-/y}$ mutants had smaller EPSCs than *Fmr1*$^{+/y}$ wild types (Figure 1C; n=17, 18 cells, p=0.0001, two-factor ANOVA on log-transformed data). Mouse N's and ages for slice physiology measurements are in Table S1. IPSCs were also reduced strongly in *Fmr1*$^{-/y}$ mutants (p=0.0001). E-I ratio, calculated as E/(E+I) in each PYR cell, was increased in *Fmr1*$^{-/y}$ mice, demonstrating that IPCSs were reduced preferentially (p=0.0001). E/(E+I) equals the fraction of excitatory to total synaptic conductance, and is termed E-I conductance ratio. *Cntnap2*$^{-/-}$ mutants showed a similar phenotype relative to *Cntnap2*$^{+/+}$ littermates, with even more prominent loss of inhibition (Figure 1D, n=12, 12 cells, p=0.0001). All individual cells are shown in Figure S1. Identical results were obtained when peak current amplitude was analyzed (Figure S2).

16p11.2$^{del/+}$ and *Tsc2*$^{+/-}$ mice showed similar phenotypes, though more modest in magnitude (Figure 1E–F). IPSCs were reduced in both mutants (*16p11.2* vs. *16p11.2*$^{+/+}$:

n=15, 12 cells, p=0.002; *Tsc2* vs. Tsc2$^{+/+}$: n=22, 15 cells, p=0.006), but feedforward EPSCs were not significantly reduced (*16p11.2*; p=0.36; *Tsc2*: p=0.17). This led to modestly increased E-I conductance ratio for both mutants (*16p11.2*: p=0.016, Tsc2: p=0.001). Overall, in *Fmr1*$^{-/y}$, *Cntnap2*$^{-/-}$, *16p11.2* $^{del/+}$ and *Tsc2*$^{+/-}$ mice, the area under the mean input-output curve for EPSCs was 0.57, 0.36, 0.86 and 0.92 of wild type respectively; for IPSCs it was 0.55, 0.18, 0.63 and 0.74 of wild type; and for E-I ratio was 2.24, 1.79, 1.29, 1.37 of wild type. Mutant and wild type PYR cells did not differ in baseline recording or stimulation parameters, or in EPSC or IPSC kinetics including latency and EPSC-IPSC delay (Table S2, Figure S1). Thus, these 4 genetically distinct ASD mutants exhibited a common impairment in feedforward IPSCs, variably coupled to a loss of feedforward EPSCs, yielding a common increase in E-I conductance ratio. This result occurred despite strain differences in wild-type currents, which likely reflect genetic background effects.

Spontaneous miniature synaptic currents (mEPSCs and mIPSCs) in L2/3 PYR cells also showed a preferential reduction in mIPSC activity compared to mEPSC activity, observed in 3 of the 4 ASD mutants (Figure S3). This suggests a broad reduction in inhibitory synapse number or function.

Spiking excitability in the L2/3 network

Does increased E-I ratio drive stronger synaptic responses and more spiking in L2/3, as commonly predicted from the E-I ratio hypothesis? To test this, we first measured spontaneous spiking in L2/3 PYR neurons in slices in low-divalent Active Ringers solution, which promotes spontaneous network activity. Cell-attached recording was used to preserve the intracellular milieu. Many L2/3 PYR cells showed spontaneous firing, which was abolished by APV+NBQX (100 μM and 10 μM; n=7 cells), showing it was driven by network synaptic activity (Figure 2A–B). We compared the distribution of L2/3 PYR firing rates in each mutant genotype versus corresponding wild type (Figure 2C; n=45–66 cells each). Surprisingly, *Fmr1*$^{-/y}$, *16p11.2*$^{del/+}$ and *Tsc2*$^{+/-}$ mutants showed normal firing rates relative to wild type, and only *Cntnap2*$^{-/-}$ showed excess spiking (p=0.033, KS test).

To understand why firing rate was largely normal in ASD mutants, we measured L4-evoked postsynaptic potentials (PSPs) and spiking in L2/3 PYR neurons. Recordings were made from a baseline Vm of −50 mV, i.e. in the just-subthreshold regime most relevant to natural, synaptically evoked spiking. For each cell, we first determined Eθ in voltage clamp, then switched to current clamp, depolarized to −50±1.3 mV and measured single-stimulus L4-evoked PSPs and spikes at 1.4x Eθ. L4-evoked spiking was rare (6.9% of all sweeps, 25.4% of all cells), and PSPs were quantified from spike-edited sweeps. Example L4-evoked PSPs are shown in Figure 2D. Strikingly, no mutant genotype showed a PSP peak (maximum depolarization) greater than wild type (Figure 2E). Instead, PSP peak was unchanged from wild type (*Fmr1*$^{+/y}$ vs. *Fmr1*$^{-/y}$: 5.3±1.0 vs. 3.6 ±1.0 mV, n= 17, 11 cells, p=0.31, Mann-Whitney test; *Cntnap2*$^{+/+}$ vs. *Cntnap2*$^{-/-}$: 5.5± 0.9 vs. 4.0± 1.0 mV, n= 13, 13 cells, p=0.15; *16p11.2*$^{+/+}$ vs. *16p11.2*$^{del/+}$: 4.5 ± 1.0 vs. 4.1 ±0.7 mV, n= 13, 18 cells, p=0.88; *Tsc2*$^{+/+}$ vs. *Tsc2*$^{+/-}$: 4.1±0.8 vs. 5.4±1.2 mV, n= 19, 10 cells, p=0.07). The mean number of L4-evoked spikes was normal in ASD mutants, with only *Tsc2*$^{+/-}$ showing a non-significant trend for more spikes (Figure 2F, Table S3). The fraction of cells that exhibited L4-evoked spiking

was also unchanged (Table S3). PSP duration was variably affected, increasing only in *Tsc2*$^{+/-}$ (p=0.003, t-test).

We applied L4 stimulus trains (5 pulses at 20 Hz) to test whether temporal summation is enhanced to drive stronger PSPs. The peak amplitude of each PSP (relative to pre-train baseline) was not altered in *Fmr1*$^{-/y}$, *16p11.2*$^{del/+}$, or *Tsc2*$^{+/-}$, and was actually weakened in *Cntnap2*$^{-/-}$ late in the train (2-way ANOVA, p=0.0015). Thus, trains did not elicit excess synaptic depolarization (Figure S4). Train-evoked spiking was normal for *Fmr1*$^{-/y}$, *Cntnap2*$^{-/-}$, and *16p11.2*$^{del/+}$, but was increased in *Tsc2*$^{+/-}$ (Figure S4). Thus, despite strong preferential loss of L4-evoked IPSCs, L4-evoked synaptic depolarization was largely normal across ASD mutants, and modest increases in spontaneous network spiking (*Cntnap2*$^{-/-}$) or train-evoked spiking (*Tsc2*$^{+/-}$) were not caused by increased L4-L2/3 PSPs.

We also examined intrinsic excitability, which can be abnormal in some ASD models independent of synaptic phenotypes (Deng et al., Neuron 2013). L2/3 PYR cells showed normal passive properties at rest, including V_{rest}, R_{input}, membrane time constant (τ_{mem}), and spike threshold and rheobase (Table S3). Intrinsic spiking excitability was variably affected across mutants, with no consistent phenotype (Figure S3).

Effects of increased E-I ratio evaluated using synaptic conductance model

To understand how reduced inhibitory currents and increased E-I ratio could yield stable PSPs and evoked spiking, we modeled how L4-evoked excitatory and inhibitory synaptic conductances (G_{ex} and G_{in}) generate PSPs in L2/3 PYR cells. For each neuron in Figure 1, we converted the EPSC and IPSC measured at 1.4x Eθ into G_{ex} and G_{in} waveforms, and then used a standard, passive parallel conductance model (Wehr and Zador, 2003) to predict the PSP that these conductances would elicit (Figure 3A–B). PSPs were modeled from a starting Vm of −50 mV to assess synaptic drive just below spike threshold. Model capacitance and resting conductance were from measured values for each genotype (Table S2). The model had no free parameters.

We first evaluated whether, in the context of general weakening of synaptic conductances (Fig. 1), the standard claim is true that stable G_{ex}:G_{in} ratio preserves net synaptic depolarization (PSP peak), while increasing G_{ex}:G_{in} ratio increases PSP peak. Modeling showed this is incorrect. Instead, equal weakening of G_{ex} and G_{in} reduces PSP peak, and further weakening of G_{in} restores it (example cell, Figure 3C). The underlying principle is shown by a simulation in which we calculated the effect of differently scaled G_{ex} and G_{in} combinations on PSP peak for each *Cntnap2* wild type cell (Figure 3D). We predicted the PSP for each cell from its measured (unscaled) G_{ex} and G_{in} waveforms, and for combinations of G_{ex} and G_{in} scaled by factors of [0, 0.1, 0.2, … 1.2]. PSP peak for the unscaled G_{ex} and G_{in} combination was defined as $PSP_{unscaled}$. PSP peak for all scaled G_{ex} and G_{in} combinations was expressed as $PSP_{diff} = PSP_{scaled} - PSP_{unscaled}$. Averaging across wild-type cells revealed a smooth contour of G_{ex}/G_{in} scaling combinations that predict no change in PSP peak ($PSP_{diff} = 0$), which we term the ‘PSP stability contour’ (Figure 3D, thick contour). This contour is above the diagonal when overall synaptic conductance weakens, indicating that G_{in} must decrease more than G_{ex} to maintain a constant PSP peak. Intuitively, the preferential reduction of G_{in} on this contour depolarizes net synaptic reversal

potential and increases driving force to precisely compensate for the loss in overall synaptic conductance.

Next, we predicted PSPs from G_{ex} and G_{in} measured in ASD mutants. The mean EPSP peak predicted from G_{ex} alone was 2.0–4.3 mV smaller in ASD mutants than wild types (Figure 4A). This was significant in *Cntnap2*$^{-/-}$, *Fmr1*$^{-/y}$ and *Tsc2*$^{+/-}$ (2.4±0.4, 6.3±1.3, 13.3±2.1 mV) vs. wild type (6.8±1.2, 9.5±1.8, 15.9±1.7 mV, all $p<0.037$, KS test), but was only a trend in *16p11.2*$^{del/+}$ (9.0±1.2 vs. 11.0±2.0 mV for wild type). Similarly, the mean IPSP peak from G_{in} alone was predicted to be 1.9–4.3 mV lower in ASD mutants (Figure 4A). This was significant in *Cntnap2*$^{-/-}$, *Fmr1*$^{-/y}$ and *Tsc2*$^{+/-}$ (1.1±0.4, 4.6±1.2, 8.6±1.1 mV) relative to wild types (5.4±1.0, 7.9±0.8, 11.9±0.8 mV, all $p<0.024$ KS test), but was a trend in *16p11.2*$^{del/+}$ (4.5±1.0 vs. 6.4±1.2 mV, $p=0.19$). Thus, reduced EPSCs and IPSCs in autism mutants predict smaller EPSPs and IPSPs near spike threshold. Combined G_{ex} and G_{in} waveforms generally predicted EPSP-IPSP sequences (Figure 4B). Peak of this overall PSP was identical between autism genotypes (*Cntnap2*$^{-/-}$ 1.6±0.4 mV, *Fmr1*$^{-/y}$ 1.9±0.3, *16p11.2*$^{del/+}$ 4.1±0.7, *Tsc2*$^{+/-}$ 3.7±0.8) and wild types (*Cntnap2*$^{+/+}$1.5±0.3, *Fmr1*$^{+/y}$ 2.1±0.6, *16p11.2*$^{+/+}$ 3.6±0.5, *Tsc2*$^{+/+}$ 2.2±0.4 mV, all $p>0.1$, KS test). Across genotypes, the average difference in PSP peak was only 0.5 mV, even though the late IPSP was generally reduced (Figure 4A–C). Thus, EPSP and IPSP reductions counteract each other to stabilize PSP peak. To test this idea more thoroughly, we determined the PSP stability contour at 1.4x Eθ for wild types of each genotype. We then plotted the mean change in G_{ex} and G_{in} magnitude observed in mutants at 1.4x Eθ (values from Figure 1, plotted as filled circles in Figure 4D). These points fell on or within 0.5 mV of the PSP stability contour from wild types. Thus, the reductions in G_{ex} and G_{in} in autism mutants are quantitatively matched to preserve synaptically-evoked peak ΔVm, not to increase it.

We validated model predictions by recording L4-evoked PSPs in L2/3 PYR cells from −50 mV baseline Vm, this time with APV present to match conditions in the parallel conductance model, which lacks voltage-dependent NMDA currents. Stimulation was at 1.4x Eθ. Results were identical to the model predictions: PSP peak was unaffected, though the late IPSP was reduced in most mutants (Figure 4E–F; Figure S5). The only exception was a moderate but non-significant trend toward reduced PSP peak in *Fmr1*$^{-/y}$, replicating the model results (Figure 4E–F).

To extend these predictions over the physiological range of baseline Vm, we also modeled PSPs elicited from −70 mV. This model predicted weaker overall PSPs in mutants relative to wild type for *Cntnap2* and *Fmr1* ($p<0.027$, KS test), but not *16p11.2* and *Tsc2*. This is expected, because low driving force on inhibition at V_{rest} means that PSPs will track G_{ex}, which is reduced in *Cntnap2* and *Fmr1* (Figure S5). Overall, the observed increase in E-I conductance ratio in these 4 ASD mutants predicts stable PSP amplitude for cells near spike threshold, and reduced PSP amplitude near V_{rest}. The only exception was a non-significant trend toward reduced, not increased, PSP amplitude in *Fmr1*$^{-/y}$ mice near spike threshold (Figure 4E–F).

L2/3 network activity and sensory coding in vivo

The results above suggest that despite substantial loss of inhibition, L2/3 spike rate may be relatively unchanged or even reduced *in vivo*. To test this, we recorded single units with laminar polytrodes in L4 and L2/3 of S1 in adult urethane-anesthetized mice (P42–92, mean P62), and measured spiking in response to calibrated whisker deflections. We tested *Cntnap2*$^{-/-}$, *Fmr1*$^{-/y}$ and *16p11*$^{del/+}$ mice and corresponding wild types (Figure 5). Recordings were made in C1–2 and D1–2 whisker columns, identified by post-hoc histological staining or multiunit tuning in L4. We interleaved deflections of 9 single whiskers to map whisker receptive fields, plus deflections of the columnar whisker at multiple velocities to measure a velocity response curve (VRC) that parameterizes the gain and sensitivity of whisker-evoked spiking (Figure 5A–B). Individual units were classified as fast-spiking (FS; putative PV interneurons) or regular-spiking (RS; putative excitatory neurons) using a spike width criterion. This criterion was validated in separate experiments in which we recorded with the same electrodes in PV-Cre::ChR2 mice, and optogenetically identified spike waveforms of PV neurons from short-latency responses to blue laser flashes (Figure 5C).

We first tested whether reduced inhibition in L2/3 of ASD mutants was reflected in FS unit spiking. Spontaneous spiking of L2/3 FS units was significantly reduced in *Fmr1*$^{-/y}$ mice and showed non-significant trends toward reduction in other ASD mutants (Figure 5D) (bootstrapped median firing rate [Hz]: *Fmr1*$^{+/y}$ 0.76, *Fmr1*$^{-/y}$ 0.40, p=0.04; *Cntnap2*$^{+/+}$ 0.99, *Cntnap2*$^{-/-}$ 0.77, p=0.83; *16p11.2*$^{+/+}$ 1.20, *16p11.2*$^{del/+}$ 0.50, p=0.08, permutation test). Mouse and unit N's are in Table S4. Whisker-evoked spiking of L2/3 FS units was measured in the VRC, which reflects feedforward activation of FS inhibitory circuits. For each genotype, population VRC data was fit with a sigmoid to quantify response threshold (the deflection velocity that evokes half-maximal response), sensitivity and maximal evoked firing rate (Figure 5E). All three ASD mutant genotypes showed significant decreases in whisker-evoked firing rate for L2/3 FS units (Figure 5E, dashed lines, p<<0.001, permutation test). This was also apparent in the median response across units (Figure 5E, solid lines), and in total whisker-evoked spikes across all velocities (median spike count: *Fmr1*$^{+/y}$ 36.03, *Fmr1*$^{-/y}$ 11.92, p=0.002; *Cntnap2*$^{+/+}$ 102.72, *Cntnap2*$^{-/-}$ 33.04, p=0.126; *16p11.2*$^{+/+}$ 43.52, *16p11.2*$^{del/+}$ 19.13, p=0.05, permutation test). Response thresholds were not altered. This common reduction in whisker-evoked spiking of L2/3 FS neurons suggests that feedforward inhibition is reduced *in vivo*.

To test whether L2/3 PYR activity was abnormal, we analyzed L2/3 RS units. Spontaneous L2/3 RS spiking was normal in ASD mutants relative to wild types (Figure 6A; bootstrapped median [Hz]: *Fmr1*$^{+/y}$ 0.58, *Fmr1*$^{-/y}$ 0.32, p=0.055; *Cntnap2*$^{+/+}$ 0.30, *Cntnap2*$^{-/-}$ 0.41, p=0.17; *16p11.2*$^{+/+}$ 0.50, *16p11.2*$^{del/+}$0.61, p=0.85, permutation test). Whisker-evoked spiking across all units in the VRC was normal in *Cntnap2*$^{-/-}$ and *16p11.2*$^{del/+}$ mice, and was actually reduced in *Fmr1*$^{-/y}$ mice relative to wild type (Figure 6B, p<<0.0001, t-test). VRC response threshold was unchanged in ASD mutants (not shown). Total whisker-evoked spikes across the VRC was not altered in any ASD mutant (median spike count: *Fmr1*$^{+/y}$ 20.14, *Fmr1*$^{-/y}$ 10.26, p=0.12; *Cntnap2*$^{+/+}$ 11.27, *Cntnap2*$^{-/-}$ 12.09, p=0.16; *16p11.2*$^{+/+}$ 25.44, *16p11.2*$^{del/+}$ 30.145, p=0.85, permutation test). The fraction of L2/3 RS

units that were whisker-responsive was also normal (*Fmr1*$^{+/y}$ 0.39, *Fmr1*$^{-/y}$ 0.53, p=0.10; *Cntnap2*$^{+/+}$ 0.26, *Cntnap2*$^{-/-}$ 0.39, p=0.24; *16p11.2*$^{+/+}$ 0.46, *16p11.2*$^{del/+}$ 0.59, p=0.19, χ^2 test) (Figure 6C), as was the mean spiking response to each unit's preferred (best) whisker (Figure 6D). Thus, whisker-evoked population firing rate in L2/3 RS cells was normal, not elevated, in *Cntnap2*$^{-/-}$ and *16p11.2*$^{del/+}$ mice, and was actually reduced in *Fmr1*$^{-/y}$ mice, despite strongly reduced inhibition in these genotypes.

For one genotype (*Fmr1*), we verified the *in vivo* L2/3 RS spiking results in juveniles (P18–22). L2/3 RS units in *Fmr1*$^{-/y}$ mice (39 units, 4 mice) had normal spontaneous firing and reduced whisker-evoked spiking in the VRC, relative to *Fmr1*$^{+/y}$ mice (37 units, 3 mice) (Figure 7A–B). Few L2/3 FS units were detected at this age. Thus, L2/3 RS spiking activity in *Fmr1*$^{-/y}$ is reduced both at ~P60 and ~P20.

Sensory tuning and firing correlations

Inhibition regulates spike timing and sensory tuning, in addition to firing rate (Gabernet et al., 2005, Wehr and Zador, 2003). We tested whether L2/3 RS units in adult mice showed deficits in these sensory coding properties, which could add noise to circuits. We found essentially no deficits in spike latency (not shown), jitter (Figure 6E) or tuning sharpness (Figure 6F) in any ASD genotype. *Fmr1*$^{-/y}$ mice show spatially broader cortical activation to single-whisker stimulation, implying a blurred whisker map (Juczewski et al., 2016, Zhang et al., 2014). Consistent with map blurring, we found that the fraction of L2/3 RS units that were tuned to the columnar whisker was lower in *Fmr1*$^{-/y}$ mice (*Fmr1*$^{+/y}$ 0.53, *Fmr1*$^{-/y}$ 0.24, p=0.024, χ^2 test) (Figure 6G). This effect was also observed as a decrease in pairwise tuning similarity (signal correlation) between simultaneously recorded L2/3 RS neurons (Figure 6H). Neither *Cntnap2*$^{-/-}$ nor *16p11.2*$^{del/+}$ mutants shared these phenotypes. Thus, sensory tuning was remarkably normal in ASD mutants, except for a blurring of the whisker map in *Fmr1*$^{-/y}$.

Inhibition also regulates local cortical firing correlations, which can impact population coding. We calculated trial-by-trial spike count correlations (noise correlations) for pairs of simultaneously recorded L2/3 PYR cells (median 6 pairs per mouse) as well as raw firing synchrony, calculated as mean correlation at 0±10 ms time lag from the spike cross-correlogram. *Fmr1*$^{-/y}$ mice showed significantly reduced noise correlations relative to *Fmr1*$^{+/y}$ controls, but *Cntnap2*$^{-/-}$ and *16p11.2*$^{del/+}$ showed no change (Figure 6I). *Fmr1*$^{-/y}$ and *Cntnap2*$^{-/-}$ mice showed a similar tendency for reduced firing synchrony vs. wild types, but this was significant only for *Fmr1*$^{-/y}$ mice (*Fmr1*$^{+/y}$ vs *Fmr1*$^{-/y}$, p=0.00027; *Cntnap2*$^{+/+}$ vs *Cntnap2*$^{-/-}$, p=0.07; *16p11.2*$^{+/+}$ vs *16p11.2*$^{del/+}$, p=0.49, permutation test) (Figure 6J). Thus, firing correlations were decreased or unchanged in ASD mutants.

Sensory-evoked spiking in L4

Sensory gain between L4 and L2/3 *in vivo* may parallel the functional strength of L4-L2/3 feedforward PSPs *in vitro*. To test this, we measured spiking of L4 RS units *in vivo*, typically recorded after L2/3 in the same penetrations. Spontaneous activity of L4 RS units was normal across all ASD mutant genotypes. Whisker-evoked spiking in the VRC for L4 RS units was normal for *Fmr1*$^{-/y}$ and *16p11.2*$^{del/+}$ mice (Figure S6). This suggests that the

effective sensory gain between L4 and L2/3 was reduced in *Fmr1*$^{-/y}$, and was normal in *16p11.2*$^{del/+}$, matching the L4-L2/3 synaptic phenotypes in these mutants. *Cntnap2*$^{-/-}$ L4 RS units had abnormally low whisker-evoked spiking (Figure S6, $p<0.007$, t-test) suggesting that sensory gain between L4 and L2/3 was increased in *Cntnap2*$^{-/-}$, perhaps related to the increased network excitability observed in active slices (Figure 2).

Spiking *in vivo* in L2/3 of awake *Fmr1* mice

Finally, we tested for excess spiking of L2/3 RS units in awake mice, using the *Fmr1* genotype, where excess S1 spikes have been reported under anesthesia (Zhang et al., 2014) but calcium imaging in awake mice suggests normal or even reduced whisker responses (He et al., 2017). We trained head-fixed *Fmr1*$^{-/y}$ and *Fmr1*$^{+/y}$ mice (n=3 each) to perform a simple visual detection task while our standard whisker stimuli (defined above) were passively presented to individual whiskers every 0.2 sec. Mice were task-engaged and licked for reward, but did not whisk. We recorded single units using laminar polytrodes from C1–2 and D1–2 columns (n=1–4 recording sessions and 10–32 L2/3 RS units per mouse). Spontaneous spiking of L2/3 RS units was unchanged between *Fmr1*$^{-/y}$ and *Fmr1*$^{+/y}$ mice (Figure 7C), but whisker-evoked spiking in the VRC was reduced (Figure 7D). The fraction of whisker-responsive units and tuning sharpness were normal (Figure 7E–F). These results closely mirror the findings in anesthetized mice, and show that excess spiking was not observed among L2/3 RS units in awake *Fmr1*$^{-/y}$ mice.

Discussion

Common increase in E-I conductance ratio

Despite its prominence, systematic tests of the E-I ratio hypothesis across different genetic forms of ASD are lacking. We provide a broad test in 4 genetically distinct ASD mouse models. We found a common phenotype of decreased L4-L2/3 feedforward inhibition and a smaller, variable decrease in feedforward excitation, yielding a common decrease in total synaptic conductance and increase in E-I conductance ratio in L2/3 PYR cells. mIPSCs were also generally reduced more than mEPSCs, suggesting a broad circuit phenotype of reduced inhibition. *MeCP2*$^{-/y}$ mice exhibit a qualitatively similar combination of strongly reduced inhibition and more modestly reduced excitation in L2/3 of visual cortex (Banerjee et al., 2016), and *Ube3a*$^{m-/p+}$ have a similar phenotype (Wallace et al., 2012). Thus, at least 5, and possibly 6 well-validated ASD mouse models share a similar loss of total synaptic conductance, loss of inhibition and increase in E-I conductance ratio in L2/3 of sensory cortex.

These results extend prior findings of reduced inhibition in *Fmr1*$^{-/y}$ mice from L4 (Gibson et al., 2008) to L2/3, and in *Cntnap2*$^{-/-}$ from hippocampus (Jurgensen and Castillo, 2015) to neocortex. It is also consistent with reduced inhibitory neuron number and PV expression in *Fmr1*$^{-/y}$ and *Cntnap2*$^{-/-}$ (Peñagarikano et al., 2011, Selby et al., 2007).

Synaptic responses and network spiking excitability are largely preserved

Elevated E-I ratio did not cause excess synaptic depolarization or spiking in L2/3 PYR cells, contrary to the standard E-I ratio hypothesis. Single L4 stimuli evoked normal-magnitude

PSPs from just-subthreshold Vm in all mutants. Responses to trains were also remarkably normal, except *Cntnap2*$^{-/-}$ where PSPs were reduced. Spiking to single L4 stimuli was normal in all mutants, and 3 of 4 mutant genotypes had normal spontaneous firing in active slices. *In vivo*, all 3 ASD mutants tested showed reduced whisker-evoked spiking of L2/3 FS units, consistent with reduced feedforward inhibition. However, spiking of L2/3 RS (presumed excitatory) units was normal in *Cntnap2*$^{-/-}$ and *16p11.2*$^{del/+}$ mice, and was reduced in *Fmr1*$^{-/y}$ mice. Thus, increased E-I ratio in the L4-L2/3 projection was associated with remarkably normal evoked synaptic responses and spiking in L2/3 PYR cells, and even with reduced spiking in *Fmr1*$^{-/y}$. Only *Cntnap2*$^{-/-}$ and *Tsc*$^{+/-}$ mutants showed any hint of increased spiking excitability, but this was not associated with altered feedforward synaptic depolarization.

Many prior *in vivo* studies in ASD mutants also show normal or reduced PYR firing rates. Spontaneous firing rate is normal in L2/3 of S1 and V1 in *Fmr1*$^{-/y}$, *Cntnap2*$^{-/-}$, *Pten*$^{-/-}$ and *Ube3a*$^{m-/p+}$ mice (Garcia-Junco-Clemente et al., 2013, O'Donnell et al., 2017, Peñagarikano et al., 2011, Wallace et al., 2017), and reduced in V1 of *MeCP2*$^{-/y}$ mice (Durand et al., 2012). Sensory-evoked spike rate and population activity are normal in L2–4 of S1 and V1 in *Fmr1*$^{-/y}$ and *Ube3a*$^{m-/p+}$ (Dolen et al., 2007, Berzhanskaya et al., 2016, He et al., 2017, Wallace et al., 2017; Goel et al., 2018), reduced in L2/3 of V1 in *MeCP2*$^{-/y}$ and *Pten*$^{-/-}$ (Banerjee et al., 2016, Durand et al., 2012, Garcia-Junco-Clemente et al. 2013) and slightly reduced in S1 in *Nlgn4*$^{-/-}$ mice (Unichenko et al., 2017). Increased sensory-evoked spiking has been observed in a small sample of hindpaw S1 neurons (Zhang et al., 2014) and in some studies in auditory cortex (Rotschafer and Razak, 2013), all in *Fmr1*$^{-/y}$. Thus, increased cortical spiking is not broadly observed in ASD genotypes. Increased network excitability is instead usually suggested by subtler phenotypes, including elevated firing correlations and longer UP states in young *Fmr1*$^{-/y}$ mice (Goncalves et al., 2013, Hays et al., 2011, O'Donnell et al., 2017), increased intra-burst spike frequency in *Shank3B*$^{-/-}$ mice (Peixoto et al., 2016), and broader sensory tuning in *MeCP2*$^{-/y}$, *Pten*$^{-/-}$, *Fmr1*$^{-/y}$ and *Ube3a*$^{m-/p+}$ mice (Banerjee et al., 2016, Garcia-Junco-Clemente et al. 2013, Juczewski et al., 2016, Wallace et al., 2017; Goel et al., 2018). *Fmr1*$^{-/y}$ mice show faster or further spread of sensory-evoked activity in S1, suggesting a blurred whisker map (Arnett et al., 2014; Zhang et al., 2014), which we also observed in the form of increased tuning heterogeneity in each S1 column.

E-I ratio is coordinated to stabilize synaptic responses near spike threshold

A simple synaptic conductance model explains why increased E-I conductance ratio does not generate stronger PSPs or more spiking in ASD mutants: In all 4 ASD genotypes, the decreases in inhibitory and excitatory conductances were precisely counter-balanced to maintain constant PSPs, for Vm just below spike threshold. This Vm range is most relevant for naturally evoked spiking, as observed during active touch sequences *in vivo* (Yamashita et al., 2013). Because driving force is less for inhibition than excitation in this Vm range, the relatively large decrease in feedforward G_{in} (to 0.15–0.57 of wild type, for the 4 ASD genotypes) and the smaller decrease in G_{ex} (to 0.35–0.92 of wild type) predict equal, opposing reductions in IPSP and EPSP amplitude. Together, these preserve PSP peak in all 4 ASD mutants (Figure 4). Simulations defined a smooth contour of G_{in} and G_{ex} reductions

that jointly stabilize feedforward PSP peak, for just-subthreshold baseline Vm (Figure 4D). The mean G_{in} and G_{ex} reduction was close to this PSP stability contour in all 4 ASD mutants, and predicted < 0.5 mV change in PSP peak. Measurement confirmed that neither L4-evoked PSPs nor spikes were significantly increased in L2/3 PYR cells in ASD mutants, despite the pronounced reduction in G_{ex} and G_{in} (Figure 4).

Thus, the common interpretation that increased E-I synaptic conductance ratio necessarily predicts increased spiking excitability in networks is incorrect. Instead, the specific increase in E-I conductance ratio offsets the decrease in total synaptic conductance in these 4 ASD genotypes to produce stable PSPs. Stable PSPs may also occur in *MeCP2*$^{-/y}$ mice, where visual-evoked G_{ex} and G_{in} are reduced to ~0.60 and ~0.45 of wild type in L2/3 PYR cells (Banerjee et al., 2016), which is numerically similar to the 4 ASD mutants tested here. Thus, functionally matched changes in Gex and Gin that alter E-I ratio but preserve PSP peak are a common theme across a diverse set of ASD genotypes.

These predictions do not account for active conductances including NMDA receptors, shunting inhibition, or changes in $GABA_A$ reversal potential which occur in young *Fmr1*$^{-/y}$, *MeCP2*$^{-/y}$, and valproate models of ASD (Banerjee et al., 2016, He et al., 2014, Tyzio et al., 2014). Despite this, these predictions explain the largely stable firing rate in S1 *in vivo* and in active slices for 3 of 4 ASD mutants. Interestingly, *Fmr1*$^{-/y}$ was the only genotype to show a trend for weaker single feedforward PSPs *in vitro* (Figures 2, 4), and this mouse also showed reduced whisker-evoked spiking in L2/3 *in vivo* (Figure 6–7). While the PSP peak remained stable in ASD mutants, the late IPSP following the peak was generally weakened (Figure 4). This suggests that temporal summation may be altered under some circumstances, although responses to stimulus trains in S1 slices were again largely normal (Figure S4).

E-I ratio and synaptic homeostasis in autism

Our results show that increased E-I conductance ratio is common across ASD genotypes, but yields stable synaptic drive and largely stable spiking, at least in L2/3 of sensory cortex. How then is elevated E-I ratio related to information processing deficits in ASD? Our results strongly suggest that E-I ratio changes are compensatory in autism (Nelson and Valakh, 2015). Both excitatory and inhibitory circuits exhibit robust homeostatic plasticity that adjusts E-I ratio to stabilize cortical firing rate (Gainey and Feldman, 2017, Turrigiano 2011). In S1, this E-I homeostasis is evident during brief whisker deprivation, which weakens L4-L2/3 inhibition more than excitation, increasing E-I ratio by a precise amount that maintains stable PSPs and spiking in L2/3 (Gainey et al., 2018, Li et al., 2014). This is virtually identical to the phenotype in ASD mutants (Figure S7). We propose that many ASD mutations alter cortical spiking activity, which secondarily engages E-I homeostasis to restore cortical firing rate. ASD symptoms may arise from imperfect homeostasis that largely normalizes firing rate but maladaptively compromises other aspects of population coding, like sensory tuning or firing synchrony (e.g., Goel et al., 2008; Goncalves et al., 2013). Elevated E-I ratio may also impair the capacity to compensate for future challenges or strong inputs (Ramocki and Zoghbi, 2008), as in audiogenic seizures (Rotschafer and Razak, 2013). This could occur in S1 with stronger or more complex tactile stimuli than

were used here, or during natural exploration or attention. E-I homeostasis may successfully preserve synaptic depolarization and spiking in sparsely active areas like S1, but may be insufficient in areas with denser input or less inhibition.

This compensatory model explains why diverse genetic mutations all alter E-I ratio, why firing rate is only modestly affected, and why G_{ex} and G_{in} changes are coordinated to stabilize PSPs. Because E-I homeostasis is a natural response to network perturbation, E-I ratio changes are expected in numerous neurological disorders, as has been observed (Selten et al., 2018). This view predicts that enhancing inhibition may be insufficient to normalize ASD symptoms in cases or brain areas where effective E-I homeostasis (i.e., that normalizes cortical spike rate) has taken place.

STAR Methods

ASD model mice were obtained from Jackson Labs ($Fmr1^{+/y}$: #004828, $Fmr1^{-/y}$: #004624; $Cntnap2^{+/-}$: #017482; 16p11.2 $^{del/+}$: #013128; $Tsc2^{+/-}$: #004686). Each strain was maintained on its own genetic background as purchased from Jackson: Fmr1 mice on a FVB background, Cntnap2 mice on C57BL/6J background, and 16p11.2 and Tsc2 mice on a mixed B6129S background. Genotyping was by PCR, using Jackson Lab protocols. Optogenetic tagging experiments were performed in PV-Cre::ChR2 mice, bred by crossing PV-Cre JAX #017320 with Ai32 JAX #024109. Mice were maintained on a 12:12-hr light-dark cycle. Mice were group-housed, and weaned at postnatal day (P) 21. Slice physiology experiments used male mice aged P17-P23. *In vivo* physiology experiments used male mice aged P42-P92. All procedures were approved by the Institutional Animal Care and Use Committee at UC Berkeley.

Slice Preparation

S1 slices (350 μm thick) from P17–23 mice were cut using standard methods in the “across-row” plane oriented 35° toward coronal from midsagittal, which allows unambiguous identification of whisker barrel columns (House et al., 2011). Cutting solution contained (in mM): 85 NaCl, 75 sucrose, 25 D-(+)-glucose, 4 $MgSO_4$, 2.5 KCl, 1.25 NaH_2PO_4, 0.5 ascorbic acid, 25 $NaHCO_3$, 0.5 $CaCl_2$. Slices were then incubated at 32°C for 30 min in standard Ringer’s solution (in mM: 119 NaCl, 2.5 KCl, 1.3 $MgSO_4$, 1 NaH_2PO_4, 26.2 $NaHCO_3$, 11 D-(+)-glucose and 2.5 $CaCl_2$; all solutions were pH 7.3, 300 mOsm, and bubbled with 95% O_2 and 5% CO_2). Slices were maintained at room temperature >30 min before recording.

In Vitro Physiology

Synaptic physiology recordings were made at 30°C in standard Ringer’s solution (2.5–3.0 mL/min). Spontaneous spiking was recorded at 35°C in Active Ringer’s solution, which was identical to standard Ringer’s except that it contained 3.5 mM KCl, 0.25 mM $MgSO_4$ and 1mM $CaCl_2$, ion concentrations that more closely resemble natural cerebrospinal fluid (Dani et al., 2005).

Whole-cell recordings were targeted using infrared DIC optics. L2/3 PYR cells were identified visually, and regular spiking was verified in current clamp. Recordings were made

using 3–6 MΩ pipettes and a Multiclamp 700B amplifier (Molecular Devices, Sunnyvale, CA). Signals were low-pass filtered (2–6 kHz) and digitized (10–20 kHz).

For voltage clamp recordings, the internal contained (in mM): 108 D-gluconic acid, 108 CsOH, 20 HEPES, 5 tetraethylammonium-Cl, 2.8 NaCl, 0.4 EGTA, 4 MgATP, 0.3 NaGTP, 5 BAPTA, 5 QX314 bromide (adjusted to pH 7.2 with CsOH, 290 mOsm). For current clamp recordings, the internal contained: 116 K gluconate, 20 HEPES, 6 KCl, 2 NaCl, 0.5 EGTA, 4MgATP, 0.3 NaGTP, 105 Na phosphocreatine. Series resistance (*R*s) was required to be < 20 MΩ prior to compensation, and was compensated 60%–80% for voltage-clamp recording. Thus, initial *R*s was typically 13–19 MΩ prior to compensation, and 3–8 MΩ during recording. Bridge balance was used in current clamp. Input resistance (*R*in) and *R*s were monitored in each sweep. Cells were discarded if membrane potential (Vm) at break-in was >−60 mV, *R*in was < 75 MΩ, initial Rs was ≥ 20 MΩ, or if *R*s or *R*in changed by >20% during recording. Vm was corrected for a 12 mV liquid junction potential.

L4 was stimulated in the center of a barrel using a bipolar electrode (0.2 ms pulses). L2/3 PYR cells were recorded radially above the stimulus site. Eθ was defined as the minimal intensity that evoked an EPSC. The accuracy of Eθ determination in each cell was ± 2.4% (95% CI), based on repeated measurements in 9 cells. Input-output curves were collected with 10s isi, and 5–6 repetitions of each stimulus intensity. EPSCs and IPSCs were quantified by area or peak, 3–23 ms post-stimulus. E-I ratio was calculated from EPSCs and IPSCs as E/(E+I). This is equal to the fraction of excitatory to total synaptic conductance, because EPSCs and IPSCs were measured with equal driving force, and scales with synaptic reversal potential. Mouse age did not correlate, over the age range tested, with evoked EPSC magnitude, IPSC magnitude or E/(E+I) in L2/3 pyramidal cells for any wild-type genotype, except for *Fmr1*$^{+/y}$ mice which showed a modest increase in E/(E+I) with age (data not shown). L4-evoked PSPs were measured from a pre-stimulus baseline Vm of −50 mV, using the “slow clamp” feature of the Multi-clamp (5 s tau). When calculating average PSP amplitude, stimulus trials containing a spike were replaced with the mean value of spike threshold for that cell. Similarly, when calculating average PSP waveform for a cell, stimulus trials containing a spike were replaced with the mean non-spike PSP for that cell, scaled to the cell’s mean spike threshold.

mEPSCs and mIPSCs were recorded in TTX citrate (1 μM) and APV (100 μM), without QX-314 in the internal, holding at −72 and 0 mV respectively. In each cell, > 200 mEPSCs and > 200 mIPSCs were detected (criteria: > 5 pA amplitude, 10–90% rise time and peak latency < 2.5 ms) and analyzed using TaroTools (Taro Ishikawa, Jikei University School of Medicine, Japan). Differences in mEPSC or mIPSC amplitude, frequency, and overall activity (quantified as amplitude x frequency within each cell) were evaluated using Mann-Whitney test (α=0.05). Cell-attached spiking was measured using loose-seal recordings in voltage clamp, with holding current at 0 pA. Intrinsic spiking excitability was measured in glutamate and GABA-A synaptic blockers (in μM: 100 APV, 10 NBQX, 3 gabazine). Rheobase was defined as the smallest positive current injection (500-ms duration) that elicited 1 or more spikes. F-I curves were measured using increasing current injections above each cell’s individually determined rheobase.

Parallel conductance model

Synaptically evoked changes in Vm (ΔVm) were predicted from L4-evoked EPSCs and IPSCs at 1.4 x Eθ using a parallel synaptic conductance model, implemented in Matlab. For each cell, we first calculated the baseline-subtracted mean EPSC at −72 mV and mean IPSC at 0 mV. G_{ex} and G_{in} waveforms were calculated as $G = I/(V_{hold}-E_{rev})$, with E_{ex} = 0 mV and E_{in}= −72 mV. G_{ex} and G_{in} were constrained to be non-negative and were smoothed (Savitzky-Golay, 1-ms window). Next, we predicted ΔVm from G_{ex} and G_{in} using the parallel conductance equation (Wehr and Zador, 2003):

$$-C(dV/dt) = G_{ex}(V_m - E_{ex}) + G_{in}(V_m - E_{in}) + G_{reat}(V_m - E_{rest}) \quad (1)$$

C was 180 pF, which was the average membrane capacitance measured across our genotypes. G_{rest} was defined as $1 / R_{input}$, where R_{input} was the average input resistance measured for that genotype in current clamp recordings (Table S2). We simulated ΔVm for cells at E_{rest} = −50 mV, in order to estimate the effect of feedforward synaptic input on V_m as a cell approaches spike threshold. V_m was calculated by integrating Eq. 1 from a starting value of V_m=−50 mV with 0.1 ms time resolution, using Euler's method[37,57]. Separate analysis was run using Erest = −70 mV.

In vivo recordings in anesthetized mice

Adult male mice were anaesthetized with urethane and chlorprothixene (1.3 g/kg and 0.02 mg in saline). Recording was not blind to genotype. A 2 mm craniotomy was made over S1. The mouse was fixed via a head post and the whiskers inserted into piezoelectric actuators. Body temperature was maintained at 36.5°C. Supplemental urethane was provided as needed. The C1, D1, C2 or D2 column was localized by intrinsic signal optical imaging or electrode mapping. A NeuroNexus recording probe (16 or 32 channels) was inserted radially via a small durotomy. The probe was advanced into L2/3, allowed to settle until stable activity was observed for 30 min, and L2/3 units were recorded. Then the probe was advanced to L4 and allowed to settle again before recording.

Recording location was confirmed either by (i) histological localization by DiI labeling in cytochrome oxidase stained flattened sections, which allow direct visualization of column boundaries, or (ii) by strong tuning for the columnar whisker in multi-unit recording in L4. L2/3 and L4 were defined by microdrive depth as 100 – 413 μm and 413–588 μm below the pia [58]. 1 recording site per layer was typically recorded. A median of 7 well-isolated single units were recorded in each animal. Recordings were typically made during the light phase of the mouse's light:dark cycle. Recording in juvenile mice (P18–22) used identical methods as for adults.

Whisker Stimuli: Calibrated piezo deflections were applied to the column-associated whisker (CW) and the 8 adjacent surround whiskers (SWs) in a 3 × 3 grid, using custom software in Igor Pro. Each whisker deflection was a ramp-hold-return (4 ms – 100 ms – 4 ms). 1.7° deflections were typically used for receptive field mapping. To measure velocity response curves, the CW was deflected at 0.6, 1.1, 1.7, 2.3, 2.9, 3.4, and 4°, with amplitude

and velocity co-varying. 75–100 repetitions of each stimulus were presented at each recording site (2–2.5 s isi).

Analysis: Recordings were amplified and bandpass filtered (Plexon Instruments PBX2/16sp-G50, × 1,000 amplification, 0.3–8 kHz bandpass) and digitized at 31.25 kHz. Noise was reduced by common average referencing. Negative-going spikes were detected using an amplitude threshold (2.8–5 s.d. of background activity), followed by a shadow period of 0.66 ms after each threshold-crossing. 1.5-ms waveforms were clipped for spike sorting. Spike clustering used UltraMegaSort2000 (Hill et al., 2011) and was blind to genotype. Clusters were excluded if they had < 600 spikes, >0.8% refractory period violations (inter-spike interval < 1.5 ms), or > 30% missed spikes (based on Gaussian fit of detected spike amplitudes relative to the detection threshold). FS and RS units were separated using a spike duration criterion of 0.55 ms peak-to-trough time.

Optogenetic identification of PV interneurons: To validate the spike duration criterion for FS units, we performed a separate series of experiments in which we optogenetically tagged PV interneurons in vivo and identified their spike waveform characteristics. These were performed in adult PV-Cre::ChR2 mice. Recording methods were exactly as described for the main *in vivo* experiments. Once the recording electrode was inserted into S1, we delivered 1–2 ms blue laser flashes (443 nm, 40 mW, CrystaLaser DL445) via an optical fiber (200 μm tip diameter) positioned in air 5 mm above the pial surface. Laser output power was adjusted for each recording site to achieve robust short-latency spiking responses from a subset of units. Units were identified as PV neurons if they exhibited light-evoked spiking at 2–5 ms latency after laser onset with a firing rate 10 standard deviations greater than their baseline firing rate.

In vivo recordings in awake mice

Mice were implanted with a lightweight chronic head post. A week later, mice began water regulation and trained operantly for water reward on the behavioral task. One behavioral session (~90 min, ~250 trials) took place each day, and mice were carefully monitored for general behavior, weight, and water consumption. At the start of each session, mice were transiently anesthetized (1.5% isoflurane), head-fixed, and the C1–3, D1–3, and E1–2 whiskers were placed in 8 piezo benders. In each 10-sec trial, mice received interleaved whisker stimuli at 0.2 s ISI. Stimuli were the same as for the anesthetized experiment, except that a 5 ms caudal ramp, 0 ms hold, 5 ms return ramp was used. Most trials were ‘NoGo’ trials in which mice were not rewarded, and generally did not lick. A subset of trials were ‘Go’ trials in which a blue LED flashed at 8.5 sec (after completion of the whisker stimuli for that trial) to indicate availability of water reward. Licks were monitored by infrared beam break and recorded. The fraction of ‘Go’ trials was adjusted daily to maximize total trial number the mouse would perform, and was typically ~50% in well-trained mice. Mice initiated trials by suppressing licking for 3 sec. Mice were trained until they achieved a hit rate of ~85% (on ‘Go’ trials) and a false alarm rate of ~10% (licks on ‘NoGo’ trials). Training took ~2 weeks per mouse.

Once the behavioral criterion was obtained, C1–2 and D1–2 columns were localized by intrinsic signal imaging, and a craniotomy was performed. Spike recordings were made during behavior from L2/3 and L4 using laminar polytrodes (as above). Spikes were sampled (24.4144 kHz), and stored (TDT RZ5D). Neural signals were bandpass filtered offline (300–6000 Hz) and common average referenced using custom Matlab code, and then spike sorted as for the anesthetized recordings. Epochs within ± 200 ms of a lick were excluded from analysis to avoid lick-related spiking in S1.

Data were analyzed from recordings whose L4 multi-unit tuning clearly matched the target whisker. RS and FS spikes were well-separated by a spike width criterion of 0.45 ms. Relatively high FS firing rates in awake mice prevented effective sorting and analysis of most FS single units, so only L2/3 RS units were analyzed.

Quantitative and Statistical Analysis

All phenotypes were evaluated by comparing each mutant genotype to its corresponding wild type strain. Differences between the wild-types strains reflect the different genetic backgrounds. For slice physiology data, statistical analyses were performed in Prism 7.0 (GraphPad). At least 2 mice and 2 separate litters were used for each measurement. Non-Gaussian data were either log-transformed for parametric testing, or nonparametric tests were applied, as specified in Results. 2-tailed tests were used, with $\alpha = 0.05$. Values in the text are mean ± SEM. Experiments were typically performed blind to genotype and conditions, except in a few cases where more animals of a specific genotype were required to balance the data set. All data analysis was done blind to experimental conditions.

For conductance modeling, predicted PSP peak was quantified as maximum depolarization within 50 ms post-stimulus. Statistical tests are indicated in the figures, and used $\alpha=0.05$. Hypothesized reductions in predicted EPSP or IPSP magnitude (strongly predicted by the voltage-clamp findings in Fig. 1) were tested by 1-tailed KS test. Changes in total predicted PSP were tested by 2-tailed KS test, because no clear prior prediction was available.

For in vivo recordings, analysis was done in Matlab. For anesthetized recordings, spontaneous firing rate was measured in each trial across multiple epochs beginning 0.7 s after stimulus offset, which is after whisker-evoked spiking or suppression has subsided. Whisker-evoked spiking was quantified during the epoch [4,50] ms after stimulus onset. For awake recordings, spontaneous firing rate was calculated from the epoch [−50,−4] ms before each whisker stimulus, and evoked firing rate from the epoch [4,50] ms following each stimulus. To determine whether a whisker evoked a significant response from a unit, we computed the probability that a Poisson process with that unit's mean spontaneous firing would generate the number of spikes measured after whisker deflection, using a binless method. For this test, we used $\alpha=0.0056$ for each whisker ($\alpha=0.05$ / 9 whiskers) for anesthetized experiments, and $\alpha=0.00625$ ($\alpha=0.05$ / 8 whiskers) for awake experiments. Units with significant response to at least 1 whisker were considered whisker-responsive. Whisker receptive field size was the total number of whiskers to which a unit was significantly responsive. The 'best whisker' (BW) was defined as the whisker evoking numerically the greatest number of spikes.

Tuning width, tuning accuracy and response latency were calculated only for whisker-responsive units. Response magnitude (e.g., in the velocity response curve) was computed across all single units, including those that were not significantly responsive. Latency was calculated from all combined spikes evoked by significant whiskers, as the earliest time bin at which evoked firing rate exceeded spontaneous firing rate modeled as a Poisson process (α=0.05). Jitter was calculated as the standard deviation of spike times 4–50 ms post-stimulus, measured across all whiskers within a unit's whisker receptive field. Tuning sharpness was defined as the firing rate evoked by the BW divided by the sum of the BW-evoked firing rate plus mean firing rate to all immediately adjacent whiskers. Response latency, jitter and unit depth were normally distributed and genotype differences were evaluated by 2-tailed t-test (α=0.05). Velocity response curve data from all units of a given genotype were combined and fit to a sigmoid function using nonlinear regression using the 'fitnlm' MatLab function, using the cauchy robust weighting option. For VRC fits, statistical differences between genotypes in parameter values were determined by t-test with α=0.007, reflecting Bonferroni correction of total α=0.05 across 7 different deflection velocities within the VRC. All other statistical comparisons were made by permutation test with α = 0.05.

Signal correlation, noise correlation and spike synchrony were calculated from all pairs of simultaneously recorded L2/3 RS neurons located < 0.2 mm apart (location inferred from the recording pad at which spike amplitude was maximal for each unit). Signal and noise correlation were calculated using Matlab's corrcoef() function. Spike synchrony was calculated from cross-correlograms generated with Matlab's xcorr() function, using 0.5 ms bin size and 'coeff' normalization to remove effects of firing rate. Synchrony was calculated as the mean cross-correlation value over ±10 ms, excluding 0 and ±0.5 ms bins where the shadow period during spike detection prevented simultaneous spikes from being recorded.

Supplementary Material

Refer to Web version on PubMed Central for supplementary material.

Acknowledgments

We thank Michael Nemeh, Michelle Ju, Theodore Huynh, Jessica Benson, Carl Shi, and Shikhar Dhingra for technical assistance, and Melanie Gainey for advice. This work was supported by the Simons Foundation (342096), NIH (R01 NS105333), the Miller Institute for Basic Research at UC Berkeley (MA), and the Ford Foundation (MA).

References

Arnett MT, Herman DH, and McGee AW (2014). Deficits in tactile learning in a mouse model of fragile X syndrome. PLoS ONE 9, e109116. [PubMed: 25296296]

Banerjee A, Rikhye RV, Breton-Provencher V, Tang X, Li C, Li K, Runyan CA, Fu Z, Jaenisch R, and Sur M (2016). Jointly reduced inhibition and excitation underlies circuit-wide changes in cortical processing in Rett syndrome. Proc Natl Acad Sci U S A 113, E7287–E7296. [PubMed: 27803317]

Bateup HS, Johnson CA, Denefrio CL, Saulnier JL, Kornacker K, and Sabatini BL (2013). Excitatory/inhibitory synaptic imbalance leads to hippocampal hyperexcitability in mouse models of tuberous sclerosis. Neuron 78, 510–522. [PubMed: 23664616]

Berzhanskaya J, Phillips MA, Shen J, and Colonnese MT (2016). Sensory hypo-excitability in a rat model of fetal development in Fragile X Syndrome. Sci. Rep 6, 30769. [PubMed: 27465362]

Chao H-T, Chen H, Samaco RC, Xue M, Chahrour M, Yoo J, Neul JL, Gong S, Lu H-C, Heintz N, et al. (2010). Dysfunction in GABA signalling mediates autism-like stereotypies and Rett syndrome phenotypes. Nature 468, 263–269. [PubMed: 21068835]

Dani VS, Chang Q, Maffei A, Turrigiano GG, Jaenisch R, and Nelson SB (2005). Reduced cortical activity due to a shift in the balance between excitation and inhibition in a mouse model of Rett syndrome. Proc Natl Acad Sci U S A 102, 12560–12565. [PubMed: 16116096]

Delattre V, La Mendola D, Meystre J, Markram H, and Markram K (2013). Nlgn4 knockout induces network hypo-excitability in juvenile mouse somatosensory cortex in vitro. Sci Rep 3, 2897. [PubMed: 24104404]

Deng P-Y, Rotman Z, Blundon JA, Cho Y, Cui J, Cavalli V, Zakharenko SS, and Klyachko VA (2013). FMRP regulates neurotransmitter release and synaptic information transmission by modulating action potential duration via BK channels. Neuron 77, 696–711. [PubMed: 23439122]

Dhamne SC, Silverman JL, Super CE, Lammers SHT, Hameed MQ, Modi ME, Copping NA, Pride MC, Smith DG, Rotenberg A, et al. (2017). Replicable in vivo physiological and behavioral phenotypes of the Shank3B null mutant mouse model of autism. Mol Autism 8, 26. [PubMed: 28638591]

Dölen G, Osterweil E, Rao BSS, Smith GB, Auerbach BD, Chattarji S, and Bear MF (2007). Correction of fragile X syndrome in mice. Neuron 56, 955–962. [PubMed: 18093519]

Durand S, Patrizi A, Quast KB, Hachigian L, Pavlyuk R, Saxena A, Carninci P, Hensch TK, and Fagiolini M (2012). NMDA receptor regulation prevents regression of visual cortical function in the absence of Mecp2. Neuron 76, 1078–1090. [PubMed: 23259945]

Elstrott J, Clancy KB, Jafri H, Akimenko I, and Feldman DE (2014). Cellular mechanisms for response heterogeneity among L2/3 pyramidal cells in whisker somatosensory cortex. J Neurophysiol 112, 233–248. [PubMed: 24740854]

Filice F, Vörckel KJ, Sungur AÖ, Wöhr M, and Schwaller B (2016). Reduction in parvalbumin expression not loss of the parvalbumin-expressing GABA interneuron subpopulation in genetic parvalbumin and shank mouse models of autism. Mol Brain 9, 10. [PubMed: 26819149]

Gabernet L, Jadhav SP, Feldman DE, Carandini M, and Scanziani M (2005). Somatosensory integration controlled by dynamic thalamocortical feed-forward inhibition. Neuron 48, 315–327. [PubMed: 16242411]

Gainey MA, and Feldman DE (2017). Multiple shared mechanisms for homeostatic plasticity in rodent somatosensory and visual cortex. Philos Trans R Soc Lond, B, Biol Sci 372.

Gainey MA, Aman JW, and Feldman DE (2018). Rapid disinhibition by adjustment of PV intrinsic excitability during whisker map plasticity in mouse S1. J. Neurosci, in press.

Garcia-Junco-Clemente P, Chow DK, Tring E, Lazaro MT, Trachtenberg JT, and Golshani P (2013). Overexpression of calcium-activated potassium channels underlies cortical dysfunction in a model of PTEN-associated autism. Proc Natl Acad Sci U S A 110, 18297–18302. [PubMed: 24145404]

Geschwind DH (2009). Advances in autism. Annu Rev Med 60, 367–380. [PubMed: 19630577]

Gibson JR, Bartley AF, Hays SA, and Huber KM (2008). Imbalance of neocortical excitation and inhibition and altered UP states reflect network hyperexcitability in the mouse model of fragile X syndrome. J Neurophysiol 100, 2615–2626. [PubMed: 18784272]

Goel A, Cantu DA, Guilfoyle J, Chaudhari GR, Newadkar A, Todisco B, de Alba D, Kourdougli N, Schmitt LM, Pedapati E, et al. (2018). Impaired perceptual learning in a mouse model of Fragile X syndrome is mediated by parvalbumin neuron dysfunction and is reversible. Nat. Neurosci 21, 1404–1411. [PubMed: 30250263]

Gonçalves JT, Anstey JE, Golshani P, and Portera-Cailliau C (2013). Circuit level defects in the developing neocortex of Fragile X mice. Nat Neurosci 16, 903–909. [PubMed: 23727819]

Goorden SMI, van Woerden GM, van der Weerd L, Cheadle JP, and Elgersma Y (2007). Cognitive deficits in Tsc1+/− mice in the absence of cerebral lesions and seizures. Ann Neurol 62, 648–655. [PubMed: 18067135]

Han S, Tai C, Westenbroek RE, Yu FH, Cheah CS, Potter GB, Rubenstein JL, Scheuer T, de la Iglesia HO, and Catterall WA (2012). Autistic-like behaviour in Scn1a+/− mice and rescue by enhanced GABA-mediated neurotransmission. Nature 489, 385–390. [PubMed: 22914087]

Harrington AJ, Raissi A, Rajkovich K, Berto S, Kumar J, Molinaro G, Raduazzo J, Guo Y, Loerwald K, Konopka G, et al. (2016). MEF2C regulates cortical inhibitory and excitatory synapses and behaviors relevant to neurodevelopmental disorders. Elife 5.

Hays SA, Huber KM, and Gibson JR (2011). Altered neocortical rhythmic activity states in Fmr1 KO mice are due to enhanced mGluR5 signaling and involve changes in excitatory circuitry. J Neurosci 31, 14223–14234. [PubMed: 21976507]

He L, Liu N, Cheng T, Chen X, Li Y, Shu Y, Qiu Z, and Zhang X (2014). Conditional deletion of Mecp2 in parvalbumin-expressing GABAergic cells results in the absence of critical period plasticity. Nat Commun 5, 5036. [PubMed: 25297674]

He CX, Cantu DA, Mantri SS, Zeiger WA, Goel A, and Portera-Cailliau C (2017). Tactile Defensiveness and Impaired Adaptation of Neuronal Activity in the Fmr1 Knock-Out Mouse Model of Autism. J. Neurosci 37, 6475–6487. [PubMed: 28607173]

Hill DN, Mehta SB, and Kleinfeld D (2011). Quality metrics to accompany spike sorting of extracellular signals. J. Neurosci 31, 8699–8705. [PubMed: 21677152]

House DRC, Elstrott J, Koh E, Chung J, and Feldman DE (2011). Parallel regulation of feedforward inhibition and excitation during whisker map plasticity. Neuron 72, 819–831. [PubMed: 22153377]

Juczewski K, von Richthofen H, Bagni C, Celikel T, Fisone G, and Krieger P (2016). Somatosensory map expansion and altered processing of tactile inputs in a mouse model of fragile X syndrome. Neurobiol Dis 96, 201–215. [PubMed: 27616423]

Jurgensen S, and Castillo PE (2015). Selective dysregulation of hippocampal inhibition in the mouse lacking autism candidate gene CNTNAP2. J Neurosci 35, 14681–14687. [PubMed: 26511255]

Li L, Gainey MA, Goldbeck JE & Feldman DE (2014). Rapid homeostasis by disinhibition during whisker map plasticity. Proc. Natl. Acad. Sci. USA 111, 1616–1621. [PubMed: 24474788]

Liang J, Xu W, Hsu YT, Yee AX, Chen L, and Südhof TC (2015). Conditional knockout of Nlgn2 in the adult medial prefrontal cortex (mPFC) induces delayed loss of inhibitory synapses. Mol Psychiatry 20, 793. [PubMed: 26098222]

Mao W, Watanabe T, Cho S, Frost JL, Truong T, Zhao X, and Futai K (2015). Shank1 regulates excitatory synaptic transmission in mouse hippocampal parvalbumin-expressing inhibitory interneurons. Eur J Neurosci 41, 1025–1035. [PubMed: 25816842]

McGuire LM, Telian G, Laboy-Juárez KJ, Miyashita T, Lee DJ, Smith KA, Feldman DE (2014). Short Time-Scale Sensory Coding in S1 during Discrimination of Whisker Vibrotactile Sequences. PLoS Biol 14(8):e1002549.

Nelson SB, and Valakh V (2015). Excitatory/inhibitory balance and circuit homeostasis in autism spectrum disorders. Neuron 87, 684–698. [PubMed: 26291155]

O'Donnell C, Gonçalves JT, Portera-Cailliau C, and Sejnowski TJ (2017). Beyond excitation/inhibition imbalance in multidimensional models of neural circuit changes in brain disorders. Elife 6.

Peixoto RT, Wang W, Croney DM, Kozorovitskiy Y, and Sabatini BL (2016). Early hyperactivity and precocious maturation of corticostriatal circuits in Shank3B(−/−) mice. Nat Neurosci 19, 716–724. [PubMed: 26928064]

Peñagarikano O, Abrahams BS, Herman EI, Winden KD, Gdalyahu A, Dong H, Sonnenblick LI, Gruver R, Almajano J, Bragin A, et al. (2011). Absence of CNTNAP2 leads to epilepsy, neuronal migration abnormalities, and core autism-related deficits. Cell 147, 235–246. [PubMed: 21962519]

Ramocki MB and Zoghbi HY (2008). Failure of neuronal homeostasis results in common neuropsychiatric phenotypes. Nature 455, 912–918. [PubMed: 18923513]

Robertson CE, and Baron-Cohen S (2017). Sensory perception in autism. Nat Rev Neurosci 18, 671–684. [PubMed: 28951611]

Rotschafer S, and Razak K (2013). Altered auditory processing in a mouse model of fragile X syndrome. Brain Res 1506, 12–24. [PubMed: 23458504]

Rubenstein JLR, and Merzenich MM (2003). Model of autism: increased ratio of excitation/inhibition in key neural systems. Genes Brain Behav 2, 255–267. [PubMed: 14606691]

Samra NM, Abdel Ghaffar HM, El Awady HA, Soltan MR and Moktader RMA (2017). Epilepsy and EEG Findings in Children with Autism Spectrum Disorders. Autism Open Access 07.

Selby L, Zhang C, and Sun Q-Q (2007). Major defects in neocortical GABAergic inhibitory circuits in mice lacking the fragile X mental retardation protein. Neurosci Lett 412, 227–232. [PubMed: 17197085]

Selimbeyoglu A, Kim CK, Inoue M, Lee SY, Hong ASO, Kauvar I, Ramakrishnan C, Fenno LE, Davidson TJ, Wright M, et al. (2017). Modulation of prefrontal cortex excitation/inhibition balance rescues social behavior in CNTNAP2-deficient mice. Sci Transl Med 9.

Selten M, van Bokhoven H and Nadif Kasri N (2018). Inhibitory control of the excitatory/inhibitory balance in psychiatric disorders. F1000Res 7, 23. [PubMed: 29375819]

Tabuchi K, Blundell J, Etherton MR, Hammer RE, Liu X, Powell CM, and Südhof TC (2007). A neuroligin-3 mutation implicated in autism increases inhibitory synaptic transmission in mice. Science 318, 71–76. [PubMed: 17823315]

Tuchman R, Cuccaro M and Alessandri M (2010). Autism and epilepsy: historical perspective. Brain Dev 32, 709–718. [PubMed: 20510557]

Turrigiano G (2011). Too many cooks? Intrinsic and synaptic homeostatic mechanisms in cortical circuit refinement. Annu Rev Neurosci 34, 89–103. [PubMed: 21438687]

Tyzio R, Nardou R, Ferrari DC, Tsintsadze T, Shahrokhi A, Eftekhari S, Khalilov I, Tsintsadze V, Brouchoud C, Chazal G, et al. (2014). Oxytocin-mediated GABA inhibition during delivery attenuates autism pathogenesis in rodent offspring. Science 343, 675–679. [PubMed: 24503856]

Unichenko P, Yang J-W, Kirischuk S, Kolbaev S, Kilb W, Hammer M, Krueger-Burg D, Brose N, and Luhmann HJ (2017). Autism Related Neuroligin-4 Knockout Impairs Intracortical Processing but not Sensory Inputs in Mouse Barrel Cortex. Cereb Cortex 1–14. [PubMed: 28365777]

Vogt D, Cho KKA, Shelton SM, Paul A, Huang ZJ, Sohal VS, and Rubenstein JLR (2017). Mouse cntnap2 and human CNTNAP2 ASD alleles cell autonomously regulate PV+ cortical interneurons. Cereb. Cortex 1–12. [PubMed: 28365777]

Wallace ML, Burette AC, Weinberg RJ, and Philpot BD (2012). Maternal loss of Ube3a produces an excitatory/inhibitory imbalance through neuron type-specific synaptic defects. Neuron 74, 793–800. [PubMed: 22681684]

Wallace ML, van Woerden GM, Elgersma Y, Smith SL, and Philpot BD (2017). Ube3a loss increases excitability and blunts orientation tuning in the visual cortex of Angelman syndrome model mice. J Neurophysiol 118, 634–646. [PubMed: 28468997]

Wehr M, and Zador AM (2003). Balanced inhibition underlies tuning and sharpens spike timing in auditory cortex. Nature 426, 442–446. [PubMed: 14647382]

Wood L, and Shepherd GMG (2010). Synaptic circuit abnormalities of motor-frontal layer 2/3 pyramidal neurons in a mutant mouse model of Rett syndrome. Neurobiol Dis 38, 281–287. [PubMed: 20138994]

Yamashita T, Pala A, Pedrido L, Kremer Y, Welker E, and Petersen CCH (2013). Membrane potential dynamics of neocortical projection neurons driving target-specific signals. Neuron 80, 1477–1490. [PubMed: 24360548]

Yizhar O, Fenno LE, Prigge M, Schneider F, Davidson TJ, O'Shea DJ, Sohal VS, Goshen I, Finkelstein J, Paz JT, et al. (2011). Neocortical excitation/inhibition balance in information processing and social dysfunction. Nature 477, 171–178. [PubMed: 21796121]

Zhang Y, Bonnan A, Bony G, Ferezou I, Pietropaolo S, Ginger M, Sans N, Rossier J, Oostra B, LeMasson G, et al. (2014). Dendritic channelopathies contribute to neocortical and sensory hyperexcitability in Fmr1(−/y) mice. Nat Neurosci 17, 1701–1709. [PubMed: 25383903]

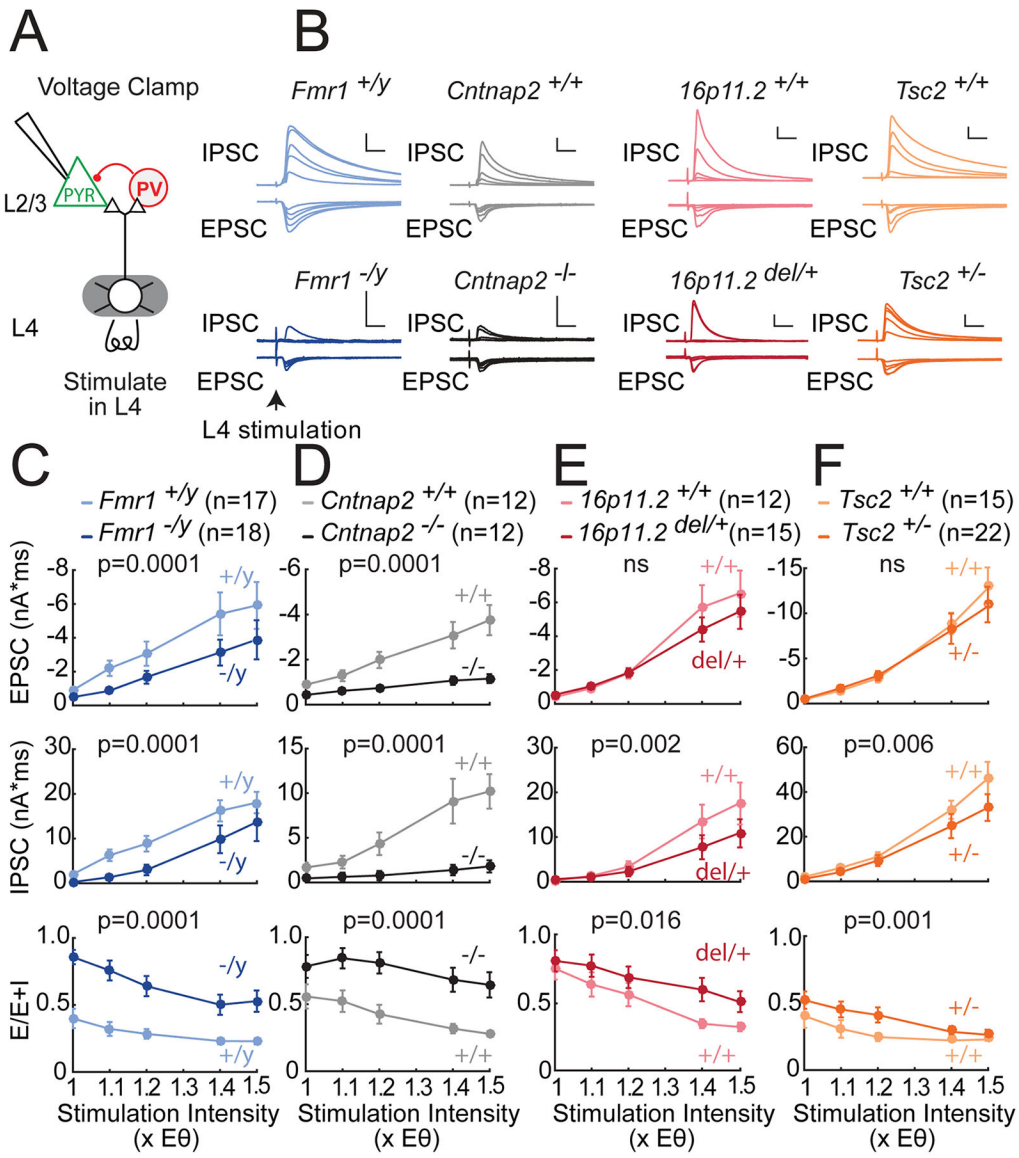

Figure 1. Deficits in feedforward excitatory and inhibitory synaptic currents in L2/3 PYR cells in four ASD mouse lines.

(A) Experimental setup to measure L4-L2/3 feedforward EPSCs and IPSCs in S1 slices.

(B) L4-evoked EPSCs and IPSCs at 1.0, 1.1, 1.2, 1.4 and 1.5x Eθ from 8 example L2/3 PYR cells from ASD mutant mice and corresponding wild types. Scale bars: 10 ms, 500 pA.

(C–F) Mean input-output curves for EPSCs, IPSCs, and E-I conductance ratio calculated as E/(E+I). Plots show mean ± SEM across cells. P-values are for genotype factor in a 2-way ANOVA on log-transformed data. N, number of cells.

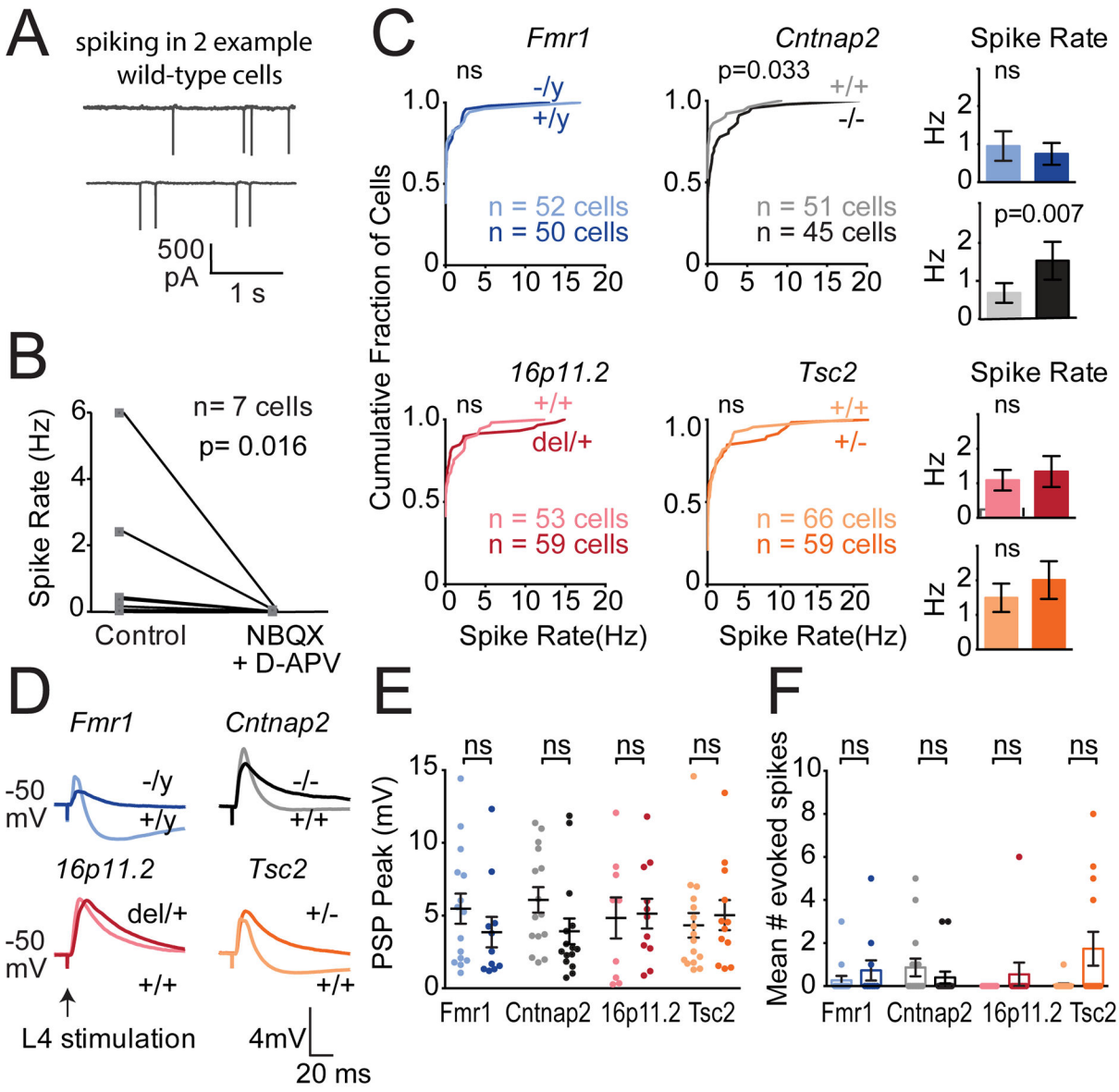

Figure 2. Spiking of L2/3 PYR cells in S1 slices.

(A) Spontaneous spiking in active Ringer's for two example L2/3 PYR cells in cell-attached mode.

(B) Spontaneous spiking is abolished by glutamate blockers (n=7 L2/3 PYR cells in 4 C57BL/6 mice). P-value from Wilcoxon matched-pairs signed rank test.

(C) Distribution of spontaneous firing rate in active slices in each genotype. Histograms show mean ± SEM of the same data. Differences were assessed by KS test. Histos have difft p-value, what test used?

(D) L4-evoked PSPs recorded in L2/3 PYR cells at 1.4x EΘ from baseline Vm of −50 mV, with NMDA currents intact. One example cell from each genotype is shown.

(E) L4-evoked PSP peak amplitude for all cells. Darker colors are ASD mutants. Each dot is one cell. Bars show mean ± SEM. 10–19 cells per genotype.

(F) Mean number of L4-evoked spikes per sweep, per cell. Each dot is a cell. Bars show mean ± SEM. Significance in (E) and (F) was assessed by Mann-Whitney test, $\alpha = 0.05$.

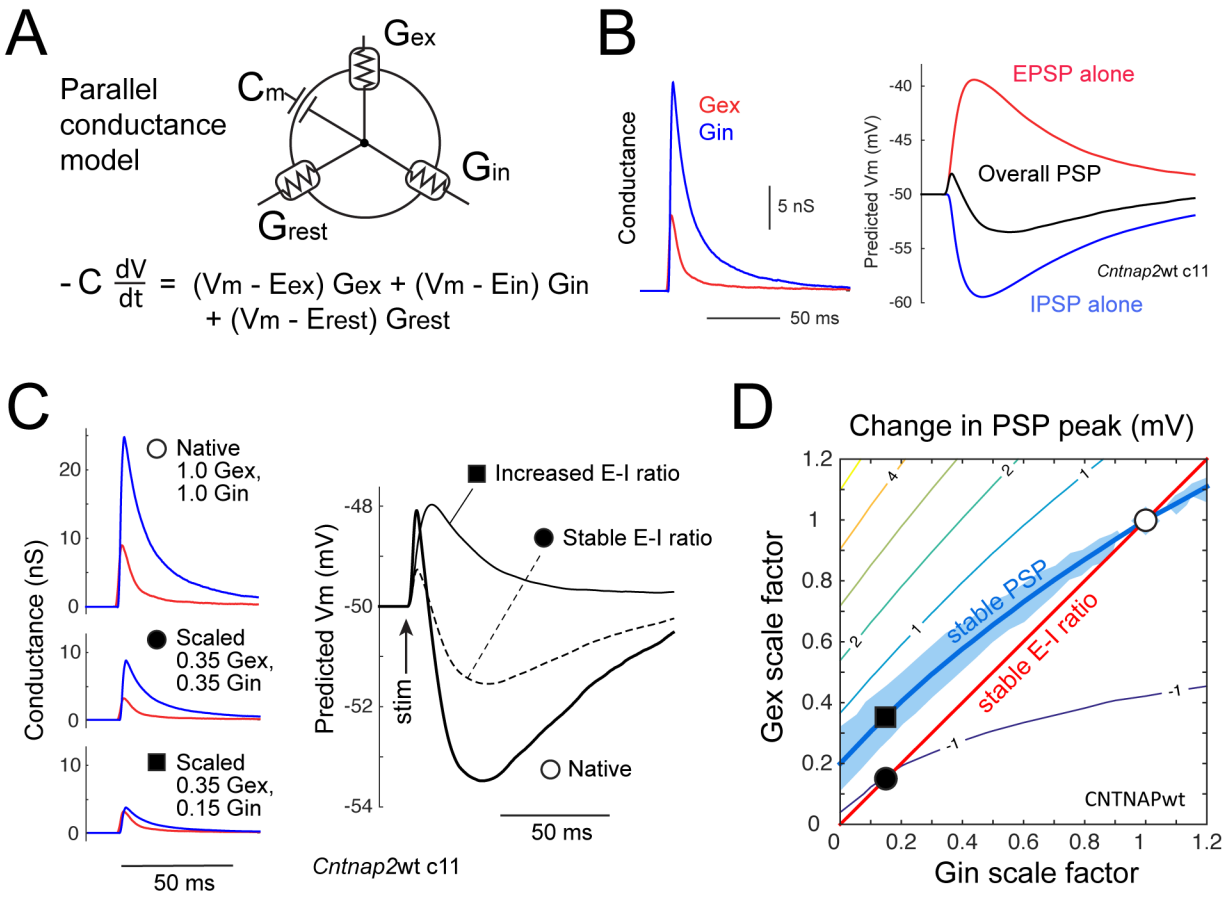

Figure 3. Relationship between E-I conductance ratio and PSP peak for cells near spike threshold

(A) Schematic of parallel conductance model.

(B) Gex and Gin waveforms for an example wild type cell, and predicted EPSP (from Gex alone), IPSP (from Gin alone), and total PSP (from Gex and Gin together) at baseline V_m = −50 mV.

(C) Conductance waveforms and predicted PSPs for one cell, for measured Gex and Gin waveforms at 1.4x Eθ (❍), after equal scaling to 0.35 of original (●), and further reduction in Gin to 0.15 of original that increases E-I conductance ratio (■).

(D) Contour plot of mean predicted change in overall PSP peak for different combinations of Gex and Gin scaling, for all *Cntnap2*$^{+/+}$ cells. Thick contour shows Gex/Gin combinations that predict no change in PSP peak (PSP_{diff}=0) from unscaled Gex/Gin. Blue region shows no significant change in PSP peak (p>0.05, bootstrap). Positive contour values denote increased predicted PSP peak. ❍ is average Gex and Gin in wild type cells. ● and ■ are from (C).

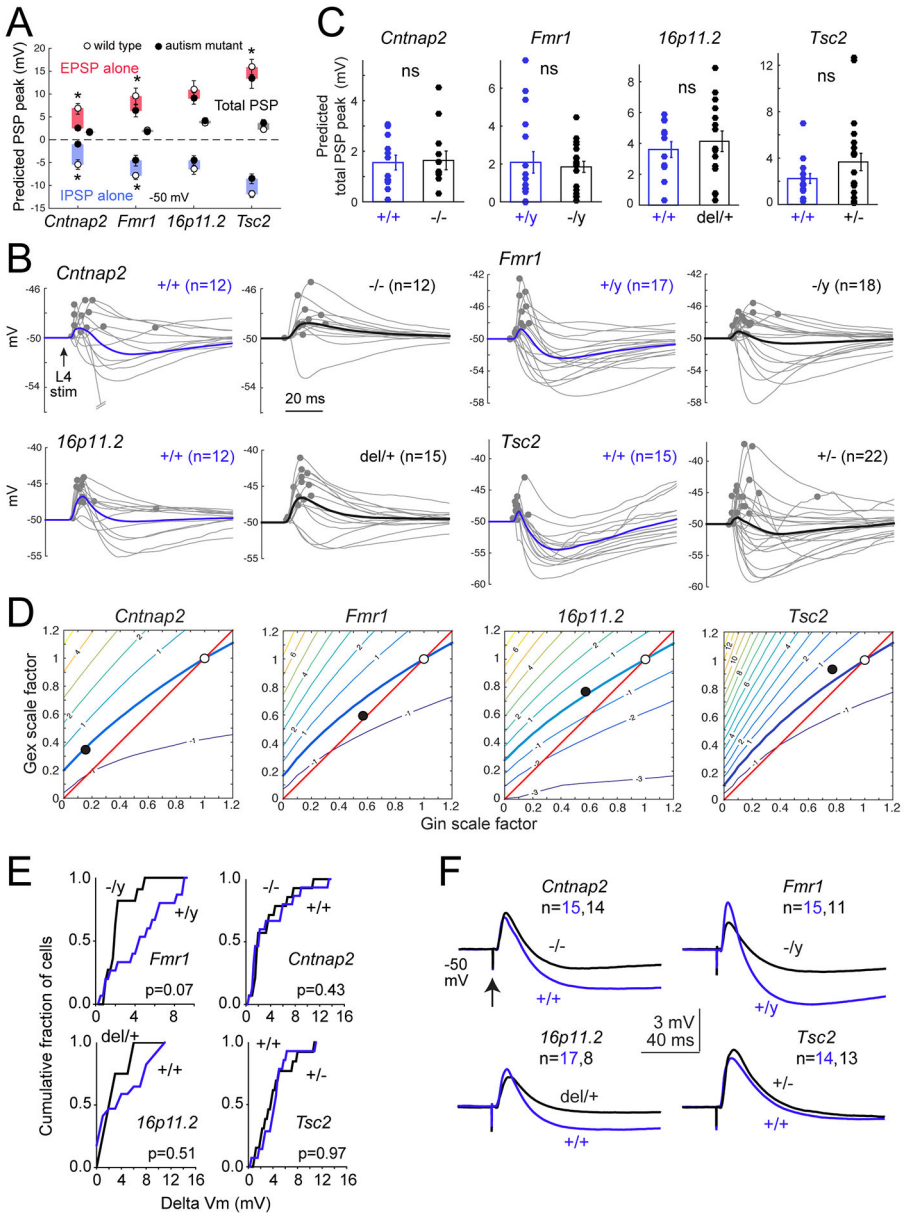

Figure 4. E-I conductance changes in ASD mutants predict stable PSPs

(A) Mean predicted EPSP, IPSP, and total PSP peak for each genotype at baseline Vm = −50 mV, for Gex and Gin recorded at 1.4x Eθ. Symbols are mean ± SEM across cells. N for each genotype is in (C). Stars, $p<0.05$, KS test.

(**B**) PSP waveforms predicted from the measured Gex and Gin in each wild type and mutant cell. Dots show PSP peak. Bold, mean predicted PSP across cells.

(C) Distribution of peak PSP for each genotype. Bars are mean ± SEM. ns, not significant by KS test.

(D) Contour plots show PSP stability contour (thick curve) for all wild type cells of each genotype. ❍, average Gex and Gin of wild type cells [(1,1) by definition]. ●, average Gex and Gin measured in mutant cells, as fraction of wild type. In all mutants, this lies within 0.5 mV of the PSP stability contour.

(E) Cumulative histograms of measured L4-evoked PSP peak across cells in each genotype from baseline Vm of −50 mV, at 1.4x Eθ, with APV in bath. There were no significant differences between any ASD mutant and its wild type. Statistics are by KS test, α=0.05.
(F) Mean PSP waveforms for the experiment in (E).

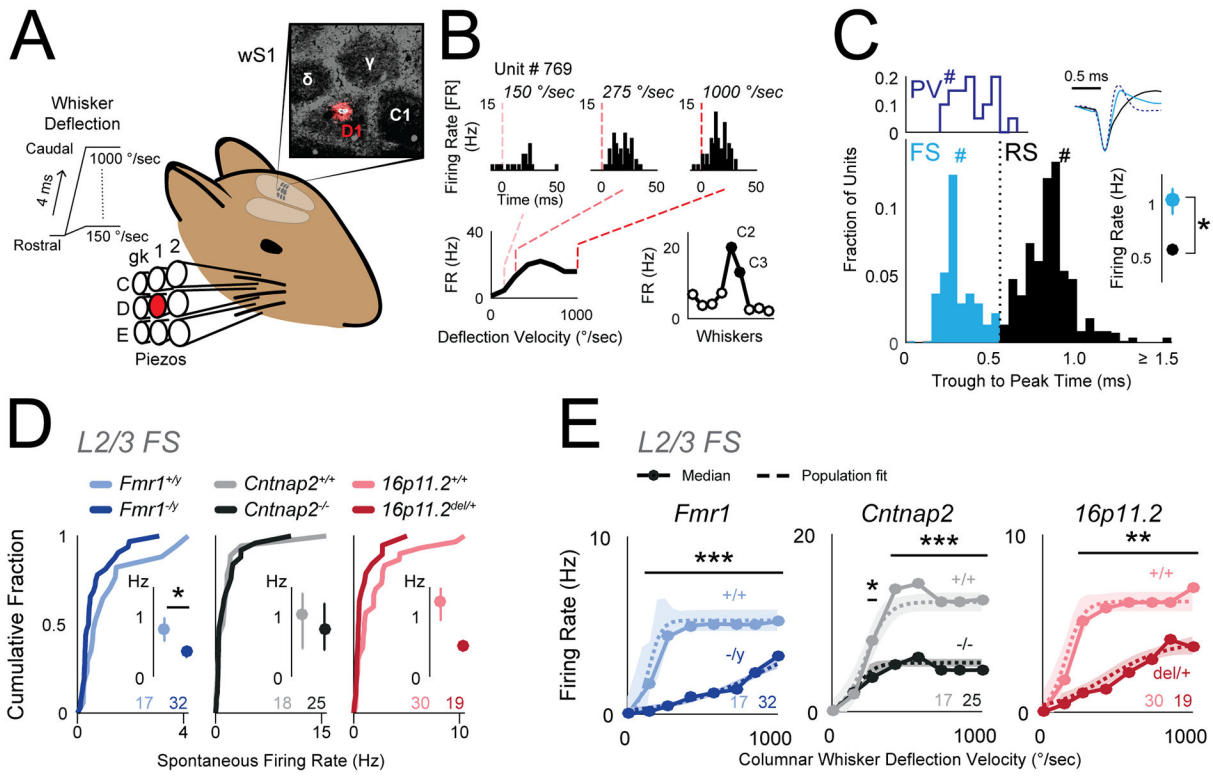

Figure 5. Reduced columnar whisker-evoked firing of inhibitory FS units in L2/3 *in vivo*

(A) Schematic for in vivo recording experiments. Deflections were delivered to 9 whiskers centered on the whisker corresponding to the recorded column in S1. Inset, D1 recording site localized by DiI labeling in cytochrome oxidase stained section of L4.

(B) Example L2/3 unit recorded in the C2 column showing responses to columnar whisker deflections at 3 velocities. Bottom, Velocity response curve (VRC; left) and whisker tuning curve (right) for this unit. Filled symbols, significant response.

(C) Top left: Trough-to-peak times for optogenetically-tagged PV neurons in PV-Cre::ChR2 mice. Bottom: Trough-to-peak times for units from ASD mutant and wild type mice. Dotted line, FS-RS threshold. Hashes mark the example waveforms (upper right). Right: Bootstrapped median firing rate for FS and RS units. Error bars are 68% CI. n = FS: [285, 69] (units, mice), RS: [546,69]. * p<0.001, permutation test.

(D) Spontaneous firing rate for L2/3 FS units, shown as cumulative distributions. Insets: Bootstrapped medians. Error bars are 68% CI. Numbers are units per genotype. * p=0.04, permutation test.

(E) Velocity response curves for the L2/3 FS unit population, calculated after subtraction of spontaneous rate for each unit. Circles: Bootstrapped population median firing rate. Dashed curve is sigmoid fit to population data. Shaded region is 68% CI. Numbers are units per genotype. * p=0.03, ** p<<0.001, *** p<<0.0001, t-test.

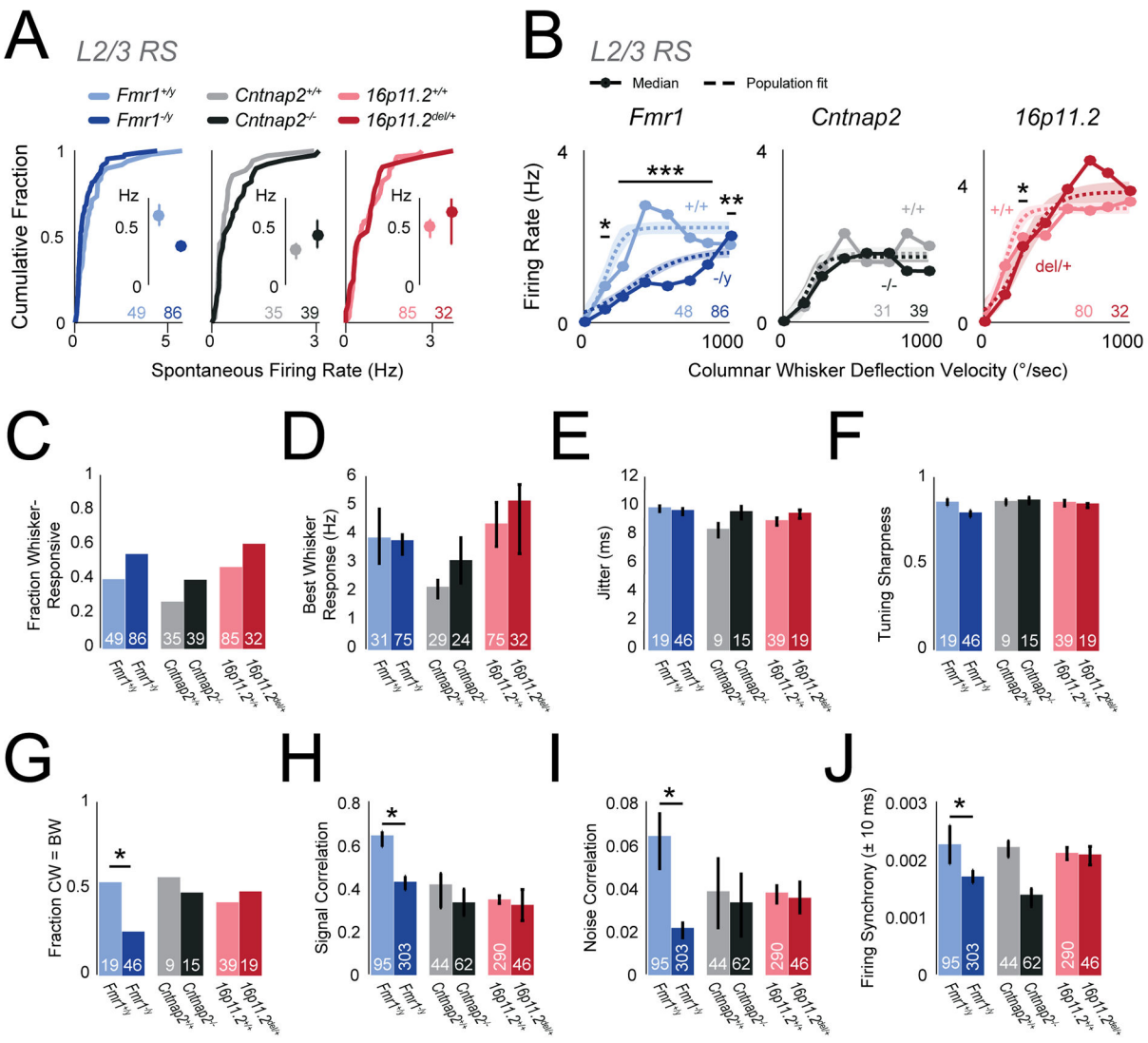

Figure 6. Firing of excitatory L2/3 RS units *in vivo* is largely normal in autism mutants

(A) Spontaneous firing rate for L2/3 RS units, shown as cumulative distributions. Insets: Bootstrapped medians with 68% CI. In all panels, numbers are units per genotype.

(B) Velocity response curves for the L2/3 RS unit population, calculated after subtraction of spontaneous rate for each unit. Circles: Bootstrapped population median. Dashed curve: sigmoid fit to population data. Shaded region is 68% CI. * p=0.01, ** p=0.001, *** p<<0.0001, t-test.

(C) Fraction of units that are whisker-responsive in each genotype.

(D) Magnitude of best whisker-evoked response (bootstrapped median with nonparametric 68% CI).

(E) Mean spike jitter for whisker-evoked responses, for whisker-responsive units. Bars are SEM.

(F) Tuning sharpness of whisker-responsive units. Bars, bootstrapped median. Error bars, 68% CI.

(G) Fraction of whisker-responsive units whose best whisker (BW) is the columnar whisker (CW). * p=0.0243, χ^2 test.

(H) Signal correlation for pairs of L2/3 RS neurons. Bars, bootstrapped median. Error bars: 68% CI. * p<<0.0001, permutation test. N is cell pairs per genotype.

(I) Noise correlation for pairs of L2/3 RS neurons. Bars, bootstrapped median. Error bars: 68% CI. * p=0.0005, permutation test.

(J) Raw firing synchrony for pairs of L2/3 RS neurons, calculated as mean over ±10 ms in the cross-correlogram. Bars, bootstrapped median. Error bars: 68% CI. * p=0.00027, permutation test.

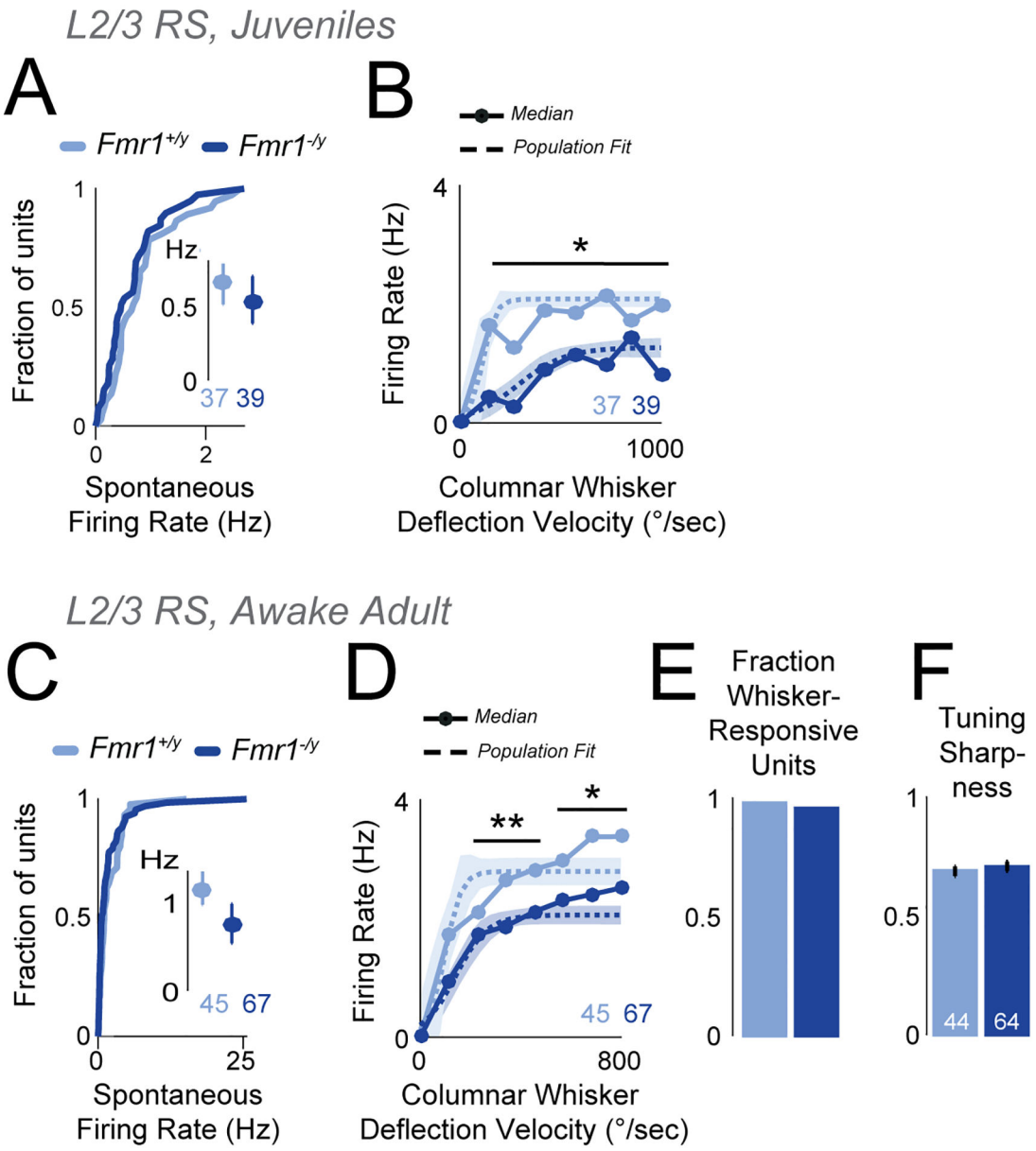

Figure 7. Firing of excitatory L2/3 RS units is reduced in anesthetized juvenile mice and awake adult *Fmr1*$^{-/y}$ mice.

(A) Spontaneous firing rate for L2/3 RS units in juvenile *Fmr1*$^{-/y}$ mice. Conventions as in Figure 6A.

(B) Velocity response curves for juvenile *Fmr1*$^{+/y}$ and *Fmr1*$^{-/y}$ mice. Conventions as in Figure 6B. * p<<0.001, t-test.

(C) Spontaneous firing rate of L2/3 RS units in awake, adult mice. Conventions as in (A).

(D) Velocity response curves for the L2/3 RS unit population in awake, adult mice. Conventions as in (B). * p=0.003. ** p<0.003, t-test.

(E) Fraction of L2/3 RS units that were whisker-responsive in awake, adult mice.

(F) Tuning sharpness of whisker-responsive units.